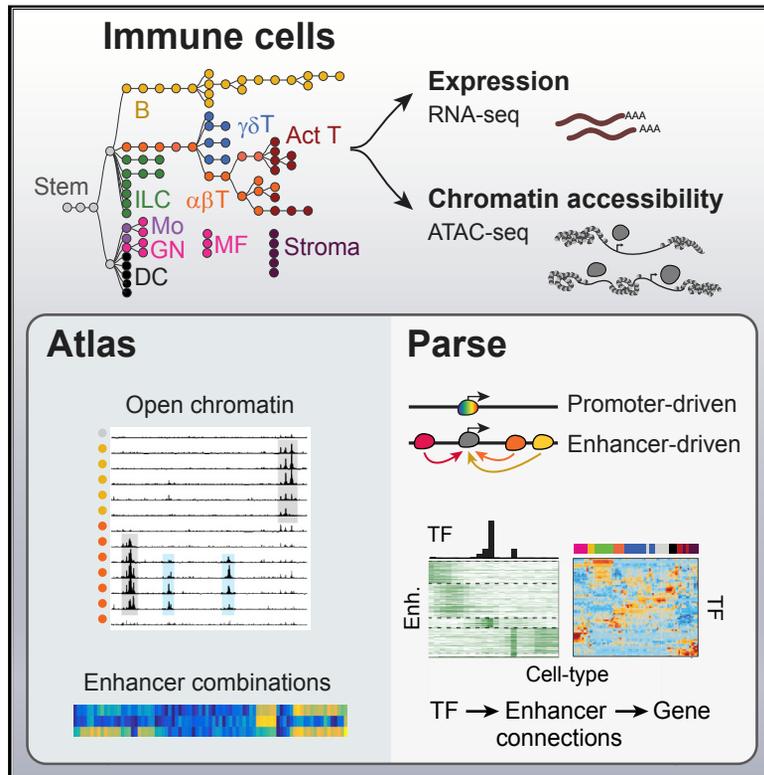# The *cis*-Regulatory Atlas of the Mouse Immune System

Graphical Abstract

Authors

Hideyuki Yoshida, Caleb A. Lareau, Ricardo N. Ramirez, ..., Jason D. Buenrostro, Christophe Benoist, the Immunological Genome Project

Correspondence

saram@stat.ubc.ca (S.M.), jason_buenrostro@harvard.edu (J.D.B.), cbdm@hms.harvard.edu (C.B.)

In Brief

A *cis*-regulatory map of the mouse immune system illuminates gene expression patterns and regulatory logic across 86 primary cell types and pairs immune transcription factors with cell-type-specific regulatory elements.

Highlights

- Atlas of 512,595 *cis*-regulatory elements active in 86 immunologic cell types

- Two classes of loci, controlled by either promoter- or enhancer-driven logic

- Inference of enhancer elements that activate each gene across differentiation

- Context-specificity of enhancer activation by transcription factors

CellPress

Resource

The *cis*-Regulatory Atlas of the Mouse Immune System

Hideyuki Yoshida,[1,2] Caleb A. Lareau,[3] Ricardo N. Ramirez,[1] Samuel A. Rose,[4] Barbara Maier,[4] Aleksandra Wroblewska,[4] Fiona Desland,[4] Aleksey Chudnovskiy,[4] Arthur Mortha,[4] Claudia Dominguez,[5] Julie Tellier,[6] Edy Kim,[7] Dan Dwyer,[7] Susan Shinton,[8] Tsukasa Nabekura,[9] YiLin Qi,[10] Bingfei Yu,[11] Michelle Robinette,[12] Ki-Wook Kim,[12] Amy Wagers,[13,14] Andrew Rhoads,[1] Stephen L. Nutt,[6] Brian D. Brown,[4] Sara Mostafavi,[15,*] Jason D. Buenrostro,[3,14,*] Christophe Benoist,[1,16,*] and the Immunological Genome Project

[1]Department of Immunology, Harvard Medical School, Boston, MA, USA
[2]YCI Laboratory for Immunological Transcriptomics, RIKEN Center for Integrative Medical Sciences, Kanagawa, Japan
[3]Broad Institute of MIT and Harvard, Cambridge, MA, USA
[4]Precision Immunology Institute, Icahn School of Medicine at Mount Sinai, New York, NY, USA
[5]Department of Cancer Immunology, Genentech, San Francisco, CA, USA
[6]The Walter and Eliza Hall Institute and Department of Medical Biology, Melbourne University, Parkville, VIC, Australia
[7]Division of Rheumatology, Immunology and Allergy, Brigham and Women's Hospital, Boston, MA, USA
[8]Fox Chase Cancer Center, Philadelphia, PA, USA
[9]Department of Microbiology and Immunology, UCSF, San Francisco, CA, USA
[10]Department of Pathology, University of Massachusetts Medical School, Worcester, MA, USA
[11]Department of Biological Sciences, UCSD, La Jolla, CA, USA
[12]Department of Pathology and Immunology, Washington University School of Medicine, St. Louis, MO, USA
[13]Joslin Diabetes Center, Boston, MA, USA
[14]Department of Stem Cell and Regenerative Biology, Harvard University, Cambridge, MA USA
[15]Department of Statistics and Department Medical Genetics, University of British Columbia, Vancouver, BC, Canada
[16]Lead Contact
*Correspondence: saram@stat.ubc.ca (S.M.), jason_buenrostro@harvard.edu (J.D.B.), cbdm@hms.harvard.edu (C.B.)
https://doi.org/10.1016/j.cell.2018.12.036

SUMMARY

A complete chart of *cis*-regulatory elements and their dynamic activity is necessary to understand the transcriptional basis of differentiation and function of an organ system. We generated matched epigenome and transcriptome measurements in 86 primary cell types that span the mouse immune system and its differentiation cascades. This breadth of data enable variance components analysis that suggests that genes fall into two distinct classes, controlled by either enhancer- or promoter-driven logic, and multiple regression that connects genes to the enhancers that regulate them. Relating transcription factor (TF) expression to the genome-wide accessibility of their binding motifs classifies them as predominantly openers or closers of local chromatin accessibility, pinpointing specific *cis*-regulatory elements where binding of given TFs is likely functionally relevant, validated by chromatin immunoprecipitation sequencing (ChIP-seq). Overall, this *cis*-regulatory atlas provides a trove of information on transcriptional regulation through immune differentiation and a foundational scaffold to define key regulatory events throughout the immunological genome.

INTRODUCTION

The establishment and maintenance of a cell's transcriptional identity is largely driven by the specific activity of *cis*-regulatory elements: promoters at which initiation complexes are assembled around RNA polymerase II (Pol-II), or distal enhancer elements that facilitate Pol-II loading and/or release from poised configuration. The time- and location-specific expression of a gene in differentiated states results from the combined activity of the several enhancers that control it, each of which may have a different regulatory logic, driven by the combinatorial activity of transcription factors (TFs) and chromatin remodelers. How enhancer activity is coordinated and integrated to define related, but functionally distinct, cell types remains elusive, leaving two main questions: How do *cis*-regulatory landscapes vary between lineage-related cell types to promote cellular identity? How do changes in the activity of *cis*-regulatory elements program the differentiation cascade of cell lineages? The mouse immune system represents an excellent setting to interrogate the interplay between epigenome and transcription: major cell states are well characterized, discrete cell populations can be readily purified, and the differentiation from common progenitors is well established, through pathways that can be parsed up to ten successive steps (Hardy and Hayakawa, 2001; Rothenberg, 2014), such that it is possible to address these questions and interrogate transitional stages at high granularity.

Previous large-scale efforts have profiled epigenomic differences across differentiation to reveal a highly diverse landscape
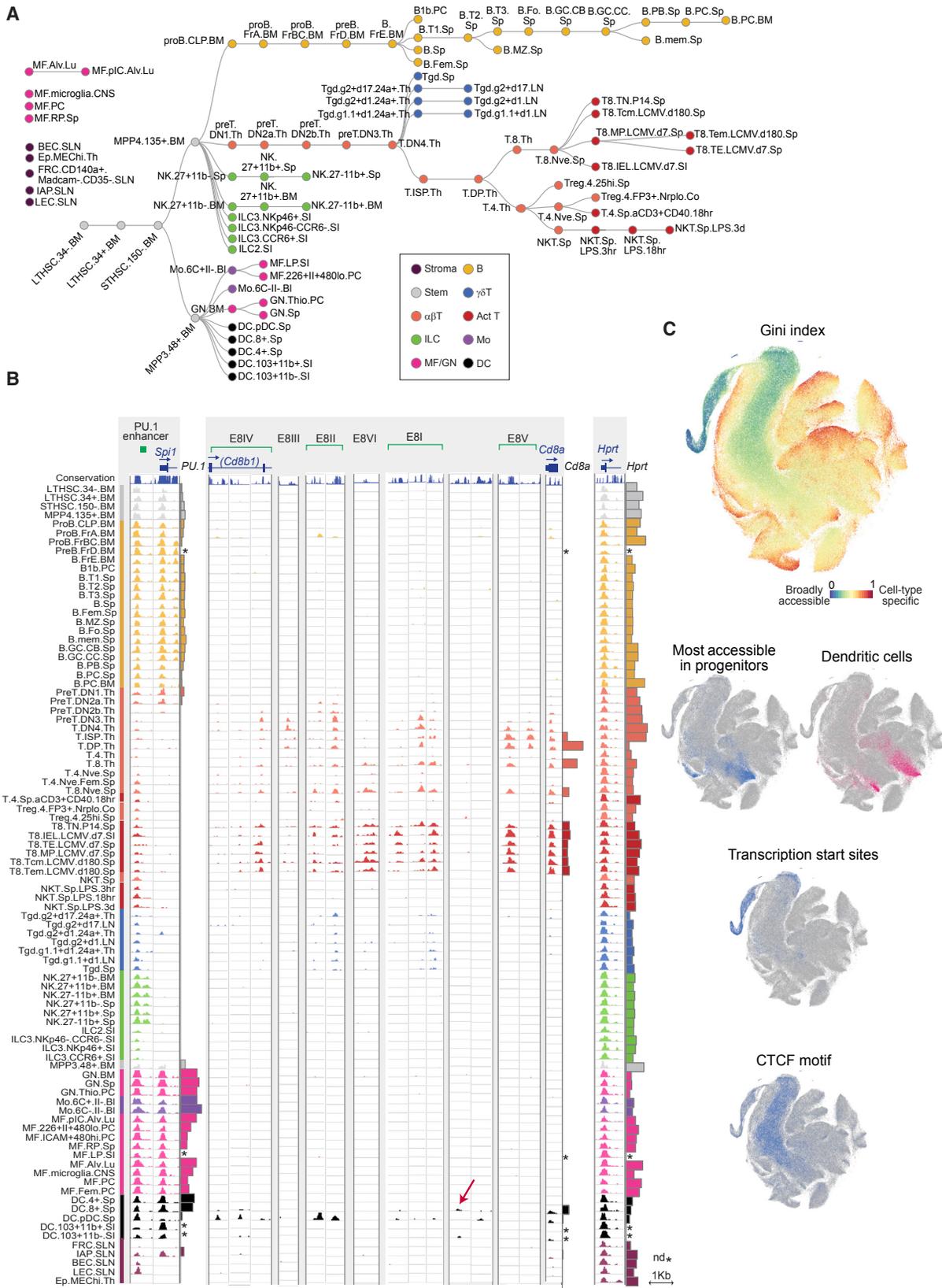
(legend on next page)

of *cis*-regulatory element activity, point to master transcriptional regulators and key *cis*-regulatory elements (ENCODE Project Consortium, 2012; Roadmap Epigenomics Consortium et al., 2015). However, these have primarily involved cell lines in culture, or whole organs that mask regulatory heterogeneity. Few large-scale programs have systematically paired epigenomic maps with gene expression measurements from primary cells, restricting the ability to infer the impact of epigenomic changes to functional consequences in gene expression. Other studies have focused on well-defined groups of cells *ex vivo* (Lavin et al., 2014; Yu et al., 2017) or run broader surveys of hematopoietic differentiation (Lara-Astiaso et al., 2014), but a *cis*-regulatory analysis that is both wide-ranging and fine-grained has not been carried out.

Here, we use low input epigenomic and transcriptomic profiling to generate matched measurements in 86 unique immune cell populations that span the entire immune system of the mouse, from granulocytes to terminally differentiated plasma cells. This atlas of open chromatin regions (OCR) is both comprehensive, defining the *cis*-regulatory space in the quasi-entirety of immunocytes, and highly granular by scanning closely related cell types. This breadth and unique coherence of these data allows us to infer the activity of *cis*-regulatory elements, assign to many TFs specific locations in shaping the unique transcriptome of each cell type, and reveal generally applicable insights on the relative roles of promoters and enhancers in differentiated gene expression.

RESULTS

We generated matched assay for transposase-accessible chromatin using sequencing (ATAC-seq) and RNA sequencing (RNA-seq) data for 86 immune cell populations, representing lymphoid and myeloid hematopoietic lineages, along with key stromal cell populations (Figure 1A; Table S1). Lymphocytes included very granular differentiation cascades along the T and B lineages, and myeloid cells included neutrophil (GN), macrophage (MF), monocyte (Mo), and dendritic cell (DC) populations stemming from either embryonic yolk sac or adult bone marrow precursors and sampled from different tissues (Guilliams et al., 2014). These cells were purified across 11 ImmGen participating laboratories, in biological duplicates (Table S1; Figure S1; http://www.immgen.org/ATAC.Sort2017.pdf).

The sorted cells were jointly processed for expression profiling by low-input RNA-seq and for chromatin accessibility analysis by fast-ATAC-seq (Corces et al., 2016), a simplified version of the original protocol (Buenrostro et al., 2013) that increases the proportion of reads within OCRs and allows lower cell inputs

(10,000 cells), important here given the rarity of many immune cell types (transitional stem or progenitor cell stages or innate-like lymphocytes [ILCs] could be analyzed). Rigorous quality control steps ensured data homogeneity (thresholds on mapped paired ends, on the enrichment of reads mapping to transcription start sites, and on depth-adjusted inter-replicate correlation). We obtained high quality ATAC-seq profiles for 86 cell types (Table S1; only mast cells failed, likely from interference by heparin). To determine the full atlas of open chromatin across the immune system, we first called OCRs in individual datasets with usual thresholds (MACS false discovery rate [FDR] 0.01), supplemented by additional OCRs identified by merging reads from related cell types. We thus identified 512,595 OCRs (FDR 0.01), whose activity index was normalized across cell types by quantile normalization (Table S2). We then parsed 14,292 OCRs connected to transcriptional start sites (TSS, RefSeq) versus 498,303 mapping to more distal locations (hereafter "distal enhancers" [DE], acknowledging that not all are necessarily true enhancers in the functional sense).

The results, a virtually complete perspective on accessible chromatin across immune lineages, present a fascinating portrait of enhancer and promoter activity (Figure 1, ImmGen Chromatin data browser). Several match known immunogenomics, but others were novel and unexpected. For example, many of the OCRs detected in the *Cd8* locus correspond to (and help position) the enhancer elements mapped in classic studies of T cell differentiation (Issuree et al., 2017): some OCRs are active prior to transcription (E-8II), others only in mature CD8^{+} T cells (E8-VI) (Figure 1B). We also identified previously unknown elements: *Cd8* expression in DCs coincides with a novel OCR specific to CD8^{+} classic DCs (cDCs) and another solely active in plasmacytoid DCs (pDCs) (Figure 1B). The difference in regulatory strategies among DCs was also visible in many other loci, e.g., the defining *Itgax* locus (encodes CD11c; Figure S2). Another example was the activity of the *Spi1* enhancer (encodes PU.1), which extinguished as expected at the DN2a-DN2b transition, coincident with commitment to T cell fate (Yui and Rothenberg, 2014)

To visualize the genome-wide diversity of OCR activity across immune cell-types, we used a T-distributed stochastic neighbor embedding (tSNE) algorithm to project every OCR into a two-dimensional space, revealing distinct substructures in the data and its variability (Gini index, Figure 1C). OCRs particularly active in a lineage naturally tended to cluster, as shown for progenitors and DCs. Interestingly, many of the OCRs mapping to TSS regions clustered together in an eccentric region of low variability, suggesting a degree of conformity within promoters as a group (many others did scatter throughout, though, denoting some


Figure 1. Overview for the Chromatin and RNA Profiling of Broad Immune Cell Populations

(A) Cell types in this study shown in a differentiation tree, color-coded by lineage. Stromal cells and myeloid cell types, known to derive from embryonic precursors, are shown unconnected to the HSC-derived tree.

(B) Representative pile-up traces of ATAC-seq signals, all to the same scale, for three genomic regions: *Spi1* (encodes PU.1), *Cd8*, with previously determined enhancer elements shown (E8I to E8VI, top, red arrows denote novel OCRs in cDCs), and the *Hprt* promoter as a housekeeping gene. mRNA levels are indicated by bar plots at the right of each locus. Asterisk (*) indicates no matching RNA-seq data.

(C) A t-SNE representation of all OCRs identified in this study. Top: the Gini index characterizes OCRs that are broadly accessible (blue) or cell-type-specific (red). Middle: OCRs specifically open in progenitors or dendritic cells. Bottom: OCRs at TSS or that contain CTCF motifs.

See also Figure S1 and Tables S1 and S2.
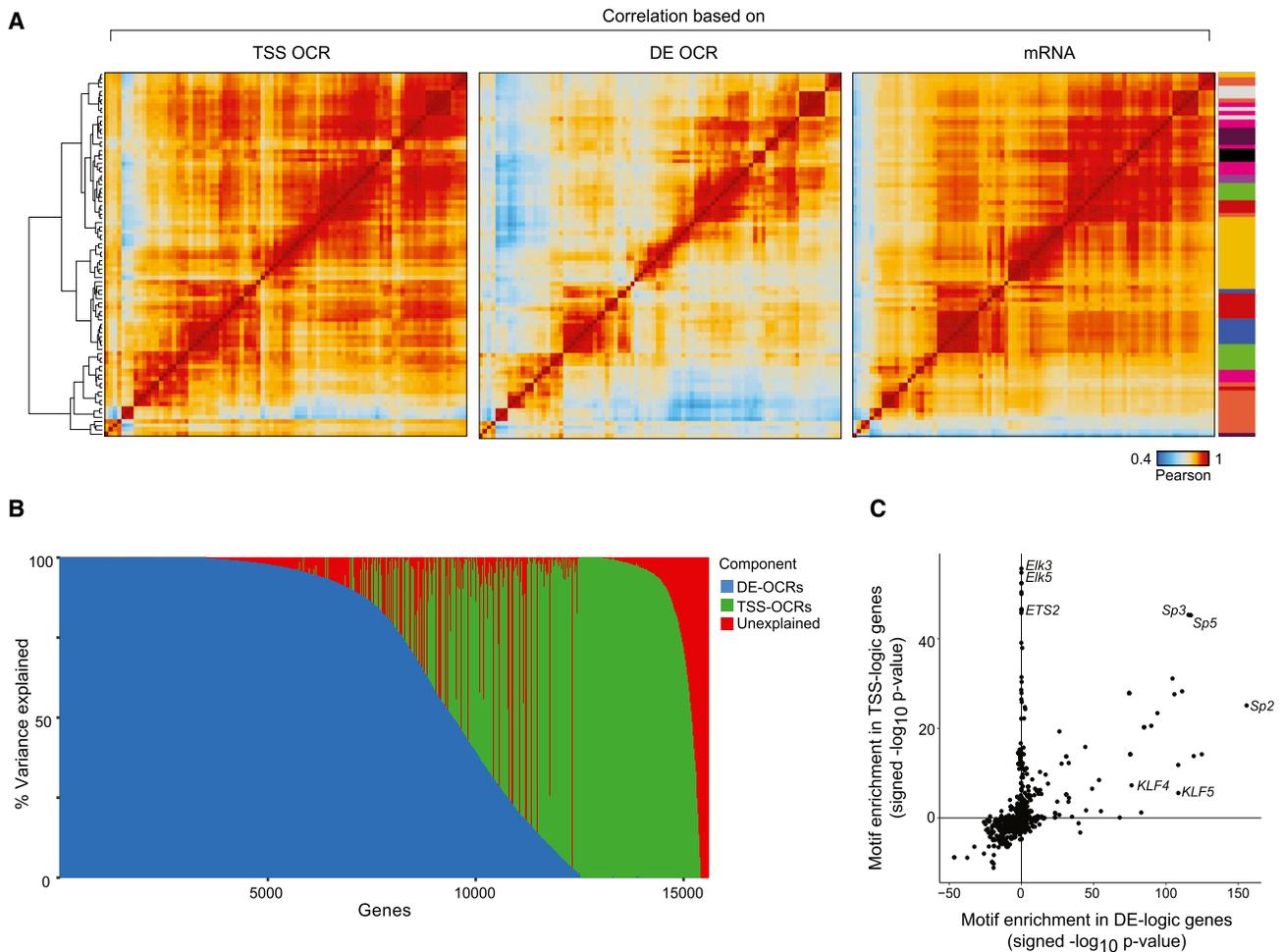
Figure 2. Integrated ATAC-RNA Variance Decomposition: Parsing Enhancer Influence

(A) Matrices of Pearson correlation between cell types, based on ATAC signal intensity at all TSS-OCR, all DE OCRs, or mRNA levels in RNA-seq. Color-coding of cell types at right per Figure 1A.

(B) Variance component decomposition of the mRNA expression for every gene (as column), in a variance component model that discretizes the explanatory power of DE- or TSS-OCRs (blue and green, respectively), the proportion of unexplained variance being shown in red.

(C) Enrichment in TF-binding sequence motifs (signed -log10 p, Fisher test) in the promoter-proximal region (−1,000 to +1 bp) of genes with DE-logic and TSS-logic determinism (from B).

See also Figure S2 and Table S3.

cell type specificity). As detailed below, we mapped the TF binding motifs associated with each OCR. OCRs associated with the structural factor CTCF, an essential anchor of chromatin loops, mapped homogeneously to a central region of limited variability. This pattern is consistent with the notion that topological domains and loops are conserved between cell lineages, even if their transcriptional activity differs (Dixon et al., 2016; Hnisz et al., 2016).

Expression Variance Explained by Chromatin Accessibility

Our extensive data provide an opportunity to determine, on a large scale, the relationship between chromatin accessibility and gene expression. In keeping with previous reports (Corces et al., 2016), cell-cell correlation matrices computed from chro-

matin accessibility at DE OCRs yielded sharper distinctions between differentiated cell types than those drawn from expression profiles (Figure 2A). Furthermore, DE OCRs showed more discrimination between cell types than TSS OCRs, consistent with the isolation and limited variance of TSS OCRs on the tSNE plots (Figure 1C).

Packaging and accessibility of DNA in chromatin are the first level of control on gene expression in differentiated cells, setting patterns that are secondarily modified by splicing or differential mRNA stability. We sought to determine how much differences in chromatin accessibility can explain differences in expression of individual genes. Variance component models, such as those used in genome-wide association and expression quantitative trait loci (eQTL) studies (Chen et al., 2016; Ye et al., 2014), can identify quantitative variables associated with relatedness

between observations by explicitly modeling sample covariance as random effects. Here, we applied an analogous concept using variance component models to quantify the proportion of variation in gene expression that could be attributed to covariance in chromatin accessibility. For each of the 15,600 expressed genes, we fit a set of variance components models, including both TSS OCR covariance and DE OCR covariance in the model, to attribute the expression levels variance of each gene to either promoter or enhancer covariance patterns. For clarification, these relationships are not between a gene and the accessibility of its own promoter or enhancers, but to the overall status of all enhancers or promoters. For most the genes, more than 90% of the expression variation could be explained, confirming that gene expression generally follows chromatin accessibility (Figure S3A; Table S3A). These results were robust with respect to the number of OCRs used in computing covariance matrices, as assessed by iterative downsampling of the OCR sets (Figure S3B). Strikingly, this analysis revealed two distinct groups of genes (Figure 2B): one for whom >99.0% of the expression variance could be best explained by TSS OCR covariance (943 genes, including *Cdca3* and *Hprt*) and a larger group (4,409 genes, including known lineage specifying genes like *Pax5* or *Foxp3*) best explained by DE OCR covariance (DE OCRs mapping to gene bodies or to extragenic regions behaved identically). This observation suggests a dichotomy between sets of active genes, whose expression follows an "enhancer logic" or a "promoter logic." These sets differed significantly in their range and variability of expression (higher and less variable for the TSS-logic set) but not in GC content (Figure S3C), with a surfeit of housekeeping and cell cycle-related genes in the TSS-logic group (Tables S3B–S3D).

This dichotomy suggested fundamentally different modes of transcriptional regulation, and we hypothesized that these groups may coopt different sets of TFs. We compared the enrichment of TF-binding motifs in the −1 kb > TSS region of the two gene sets (a span that would encompass the promoter and some proximal enhancers). Members of the ETS-ELK family were more associated with TSS-logic genes, while members of the KLF family were over-represented in the promoters of genes of the DE-logic group (Figure 2C; Table S3E). Altogether, these results suggest that gene expression in differentiated mouse immunocytes is cued by global patterns of chromatin covariation but follows two different modes.

### *cis* Regulation of Gene Expression: Linking Enhancers to Genes

One of the recurring difficulties in mapping enhancer elements is in establishing the link between a regulatory element and the gene(s) it regulates. Although enhancers often map inside or within a few kb of genes they regulate, and "closest gene" is often taken as a rough proxy to hypothesize an enhancer's target, there are documented instances of enhancers mapping megabases away from their target gene (Bahr et al., 2018). We hypothesized that correlation across cell types between the accessibility of an enhancer and the expression of a given gene denotes a functional connection, a determination facilitated by the unique breadth and granularity of the present data. For illustration, such a correlation could be detected be-

tween the expression of *Samd3* and accessibility of an OCR located 1,320 bp upstream of its TSS (Figure 3A). This correlation extended genome-wide (Figure 3B; Table S3F). By globally assessing correlation between accessibility and expression, we identified at least one significantly associated *cis* OCR within a 1 Mb window from the TSS for 7,444 of the 15,601 expressed genes (Bonferroni p < 0.05). Predictably, the remaining genes that were not associated with a *cis* OCR were enriched in the set of TSS logic genes identified above (p < 10^{-20}). These correlated OCRs preferentially mapped in the close vicinity of the correlated gene (50% of best correlated OCRs are within 13 kb of the gene's TSS), in essence vindicating the usual approach, with an exponentially decaying relationship between distance and correlation (Figure 3C). Given this observation, to reduce the number of spurious associations, we restricted our further analysis to 334,879 OCRs that fall within 100 kb of some TSS. In many instances, each gene was associated with several significantly correlated *cis* OCRs (Figure 3D), including some highly complex regions with multiple associations such as the *Il7r* locus, correlated to 21 nearby OCRs (Figure 3E). For these genes with multiple correlated OCRs, the OCRs tended to be correlated to each other (64% of the OCRs correlated with one gene were themselves correlated [at Bonferroni p < 0.05]). These multiple OCRs likely represent repeated regions that operate with the same regulatory controls.

In other instances, genes were surrounded by OCRs with clearly different patterns of activity. An anecdotal but striking example was noted upstream of *Rag1-Rag2*, where two distinct OCRs are activated in tight connection with the appearance of *Rag* transcripts in either B or T cells (Figure 3F), suggesting that T and B lineages have different solutions to tightly control B or T expression. We thus sought to broadly identify sets of independent OCRs for each target gene, using the ability of stepwise regression to identify independent explanatory variables. For a substantial number of genes (n = 493), two or more independent signals were identified in the 100 kb regions (Figure S3D; Table S3G). These "secondary" OCRs may contain cell-specific regulatory elements to fine tune expression in different lineages. For example, in the *Tyrobp* locus (encodes DAP12), the regression identified a second OCR associated with expression in the B cell lineage, and a third active in natural killer (NK) cells (Figure 3G). Around *Cd28*, an OCR whose range of activity includes plasma cells (likely related to CD28 function there) (Delogu et al., 2006) is complemented by another OCR uniquely active in T cells (Figure 3H).

Timing of OCR Activation during Lymphocyte Differentiation

We then investigated more closely the changes in OCR activity that accompany T and B lymphocyte differentiation, attempting to track changes in regulatory elements that underlie these multistep cascades. At the two main cell-specific loci in the T lineage, *Cd4* and *Cd8*, classic analyses have mapped a number of functionally important enhancer elements (Issuree et al., 2017). As noted above, several of the OCRs at the *Cd8* locus showed activity in the differentiation series prior to the appearance of *Cd8a* transcripts (i.e., E8-I and E8-II in DN3 and DN4). OCRs were also found at several known enhancer elements of *Cd4*, with the
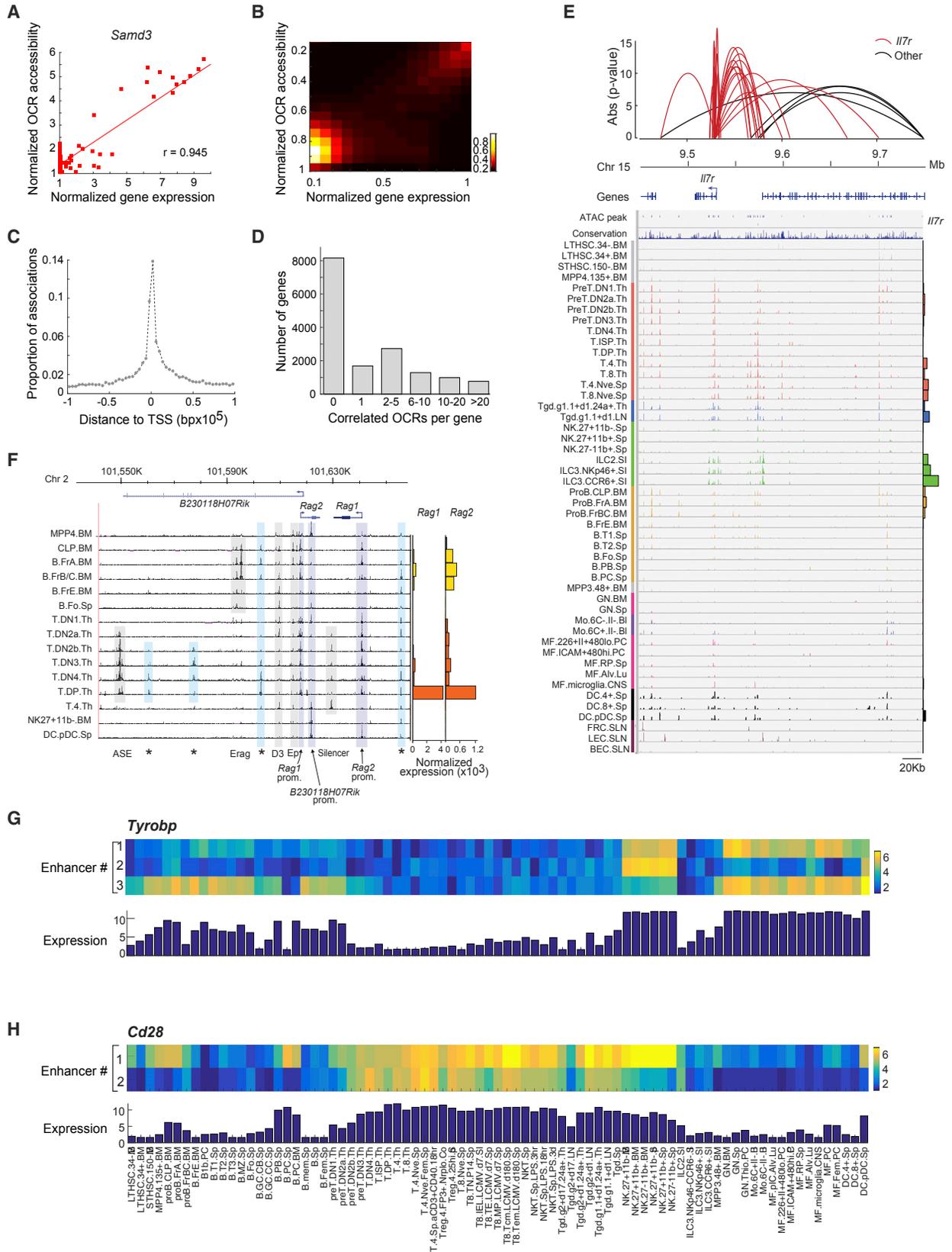
(legend on next page)

expected timing of activation (e.g., E4T, E4p, and E4D) (Issuree et al., 2017) (Figure S4A). The S4 silencer was accessible in mature CD8^{+} T cells, indicating that silencing here is likely an ongoing process. Several hitherto unrecognized elements were also observed (Figure S4A), whose function begs to be elucidated: an OCR very close to the S4 silencer and specifically active in CD4^{+} cells and several OCRs active in cDC or pDCs.

To consider more generally how OCR opening relates to changing gene expression, we selected a broad set of transcripts that are stably induced or extinguished during T differentiation, most at the point of T cell fate commitment (DN2a/DN2b) (Yui and Rothenberg, 2014), or at CD4^{+}CD8^{+} "double-positives" (DPs) (Figure 4A). Aggregating DE OCR accessibility in a 10 kb window around the TSS (but excluding TSS OCRs and constitutively accessible DE OCRs) showed that this aggregate accessibility largely tracked with gene expression (Figure 4B); in contrast, there was little relation with accessibility at these genes' TSS (not shown). Thus, the T cell differentiation cascade also seems to follow an enhancer-driven logic, rather than a TSS-driven one. Bolstering the significance of these correlated OCRs was that they showed significant enrichment in binding motifs for TFs known to be involved in controlling T differentiation (Figure S4B) such as Tcf12(HEB), Lef1, Tcf7(TCF-1), and Tcf3(E2A).

We then investigated the dynamics of OCR activation, asking whether the early enhancer activation relative to transcription observed with several Cd8 enhancers is a general rule. We compared the differentiation stage at which a given gene's mRNA level, or the accessibility at its most correlated OCR, reach 50% of their maxima (and conversely drop to 50% or their initial max for repressed loci). Strongly skewed patterns were observed, wherein OCRs mainly became open before the onset of transcription (Figure 4C). Genes whose expression increased sharply at the DP stage already had active enhancers after the DN2a > DN2b transition, while activation of expression at the time of positive selection to T4 single-positives was foretold by activation of their enhancers in late DN stages. Thus, consistent with prior observations in early B and myeloid differentiation (Mercer et al., 2011), turning on enhancers precedes the actual activation of the loci at several steps in T cell differentiation.

trans Regulation: TF Effects on Chromatin Accessibility

Paired epigenomic and transcriptomic data across a large set of cell types provides a powerful opportunity to relate epigenomic variation to the activity of specific TFs, by correlating the activity of an OCR to the TF binding sites (TFBS) it contains. To identify cell- and lineage-specific TFs that may influence chromatin accessibility, we first mapped TFBS present in each of the 334,879 robust OCRs (curated TFBS list from CisBP, per Schep et al. [2017]; Table S4 for TF motifs associated to each OCR at p < 0.1). We compared the aggregate accessibility in each cell type of all OCRs containing a given motif, relative to a background set of OCRs matched in %GC and average accessibility (Schep et al., 2017). This deviation analysis, which yields a "TFBS accessibility score" for each TF motif in each cell type, identified 76 TF motifs significantly associated with chromatin accessibility differences (Figure 5A).

TFs of the same family tend to bind the same or similar motifs (e.g., Gata family members all bind the canonical Gata motif). To disambiguate the relationship between the accessibility of a motif and the actual TFs that binds it, we compared the TFBS accessibility score to the expression of the corresponding TFs. For some like Pax5, the key regulator of B cell differentiation, there was a simple correlation between expression of the TF and the accessibility of its motif (Figure 5B). For Tbx21 (encodes T-Bet, Figure 5C) the relationship was less linear, the motif only becoming accessible at the highest expression levels, possibly denoting dose-dependence, cofactor requirement, or competitive displacement effects. This analysis also identified several repressive relationships: Pbx1, a negative regulator of stem cell differentiation (Ficara et al., 2008), and Zbtb7b, the classic repressor of the CD8-lineage transcriptome in CD4^{+} T cells (Wang et al., 2008) both showed decreased accessibility of their motif at higher TF expression (Figures 5D and 5E). In other cases, by calculating the similarity of the TF motifs used, we defined pairs of TFs that cooperate to modulate the accessibility of target enhancers. For instance, the hematopoietic regulator Bcl11a correlated positively with accessibility of the Bcl11a motif, but Bcl11b, which shuts down the B or myeloid differentiation potential in early thymic progenitors, negatively correlated with accessibility (Figure 5F).

Such correlations between accessibility and expression were generalized to all TFs with associated TFBS accessibility scores (Figure 5G), identifying 61 activators and 18 repressors (Table S5) confirmed by permutation analysis (Figure S5A). The expression of these chromatin accessibility regulators (Figure 5H) paints a uniquely rich portrait of immune cell differentiation, with regulators that appear to act individually (Eomes, Pax5) and are uniquely correlated to activity of OCRs that contain their

Figure 3. Landscape of cis-Regulation: Associating Genes with Specific Enhancers

(A) Example of correlated mRNA expression (x axis) and OCR accessibility (y axis) at the Samd3 locus.

(B) As in (A), but correlation between expression and activity of a strongly associated DE-OCR for 1,000 genes.

(C) Distance distribution of DE-OCRs that are strongly correlated (Bonferroni p < 0.05) to a given gene, relative to the gene's TSS.

(D) Number of significantly associated DE-OCRs for each gene.

(E) Chromatin accessible landscape of the Il7r locus for all cell types (histogram of expression at right). Red arcs correspond to 21 OCRs that share significant correlation with Il7r expression; non Il7r associations are shown in black (height reflects association p value).

(F) ATAC-seq signal in the promoter and enhancer regions of Rag1 and Rag2 loci in B and T precursors (right: mRNA expression). Previously reported DNase-I hypersensitivity sites are indicated below. Asterisk (*) indicates newly identified OCRs.

(G and H) Identification by multiple regression of OCRs that complementarily explain the expression patterns of (G) Tyrobp and (H) Cd28. Heatmaps denote accessibility at these OCRs; the bar histogram denotes mRNA expression.

See also Figure S3 and Table S3.

A

Normalized gene expression
(498 genes)

B

Integrated enhancer-OCR
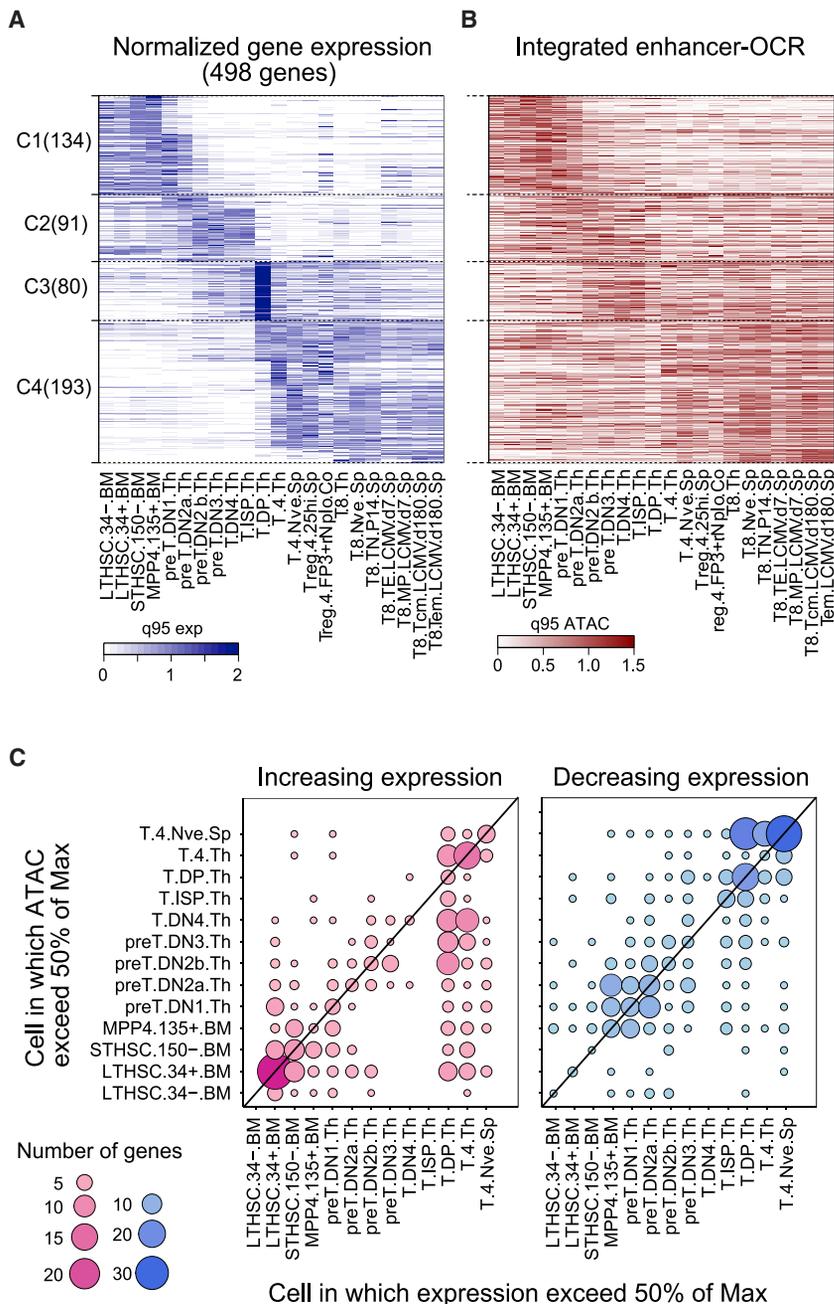
Figure 4. Timing of OCR Activation

(A) Heatmap representing expression of 496 genes that vary most through T cell differentiation (ordered by k-means, color-coded relative to the 95th expression quantile).

(B) Integrated accessibility of variable DE-OCR in the −10 kb > −250 bp region of these genes (order as in A).

(C) Timing of enhancer activation: for genes that are induced during T differentiation, the dots denote the cell stage at which mRNA expression first reaches 50% of max (x axis) versus the stage at which the best correlated OCR (from Figure 3) first reaches 50% of max accessibility.

See also Figure S4.

**C**

Increasing expression   Decreasing expression

Transcriptional Regulation in Myeloid Cells

Having broadly characterized the *trans* regulatory relationships between TFs and OCRs, we looked more specifically at OCR activity patterns in the myeloid compartment. Previous studies profiled the epigenomic state of tissue resident macrophages and other myeloid cells (Bornstein et al., 2014; Lavin et al., 2014), but the breadth of the present data provided additional perspective. Clustering of myeloid cells based on OCR activity grouped them largely according to lineage and tissue residency (Figure 6A; Table S6). There was differential OCR activity between resident macrophages of different tissues, consistent with prior reports (Lavin et al., 2014). GN and pDCs were more distant from other myeloid lineages, somewhat unexpectedly for pDCs, as they are closely related with cDCs (Reizis et al., 2011). Indeed, pDCs had a high number of distinct OCRs from cDCs and other myeloid cells, and pDCs were more similar to T cells for *Cd8* OCRs (Figure 1B), supporting the proposition that pDCs arise from a spectrum of progenitors with myeloid and lymphoid potential (Reizis et al., 2011).

A major question in myeloid biology is what factors drive the programs of closely related but functionally distinct cells. We used the TFBS resource described above to identify motifs enriched in OCRs uniquely active in certain cell types (Figure 6B). Several enriched motifs corresponded to TFs with established roles. For example, the binding motif for Tcf4 (encodes E2-2) was among the most enriched in pDCs, and E2-2 has an essential role in pDC biology (Cisse et al., 2008). Enrichment of critical tissue macrophage regulators was apparent: Gata6 in peritoneal cavity (PC) macrophages (Rosas et al., 2014) and Mef2c in microglia (Deczkowska et al., 2017; Lavin et al., 2014). These served as useful validations, we also noted a number of novel associations that may

motifs and regulators that operate interchangeably to regulate a common motif such as Runx1/2/3, which all promote accessibility of the Runx motif. Some TFs are expected to be refractory to such an analysis and showed no such correlation: FoxP3 because of its binding to previously open elements (Samstein et al., 2012), Nfatc1 because its regulation is based in intracellular localization rather than abundance, and Stat1 because the present dataset may poorly capture its rapid induction. With this reservation, this integrated approach enabled us to define some of the key TFs that positively or negatively shape chromatin accessibility in immune cells.
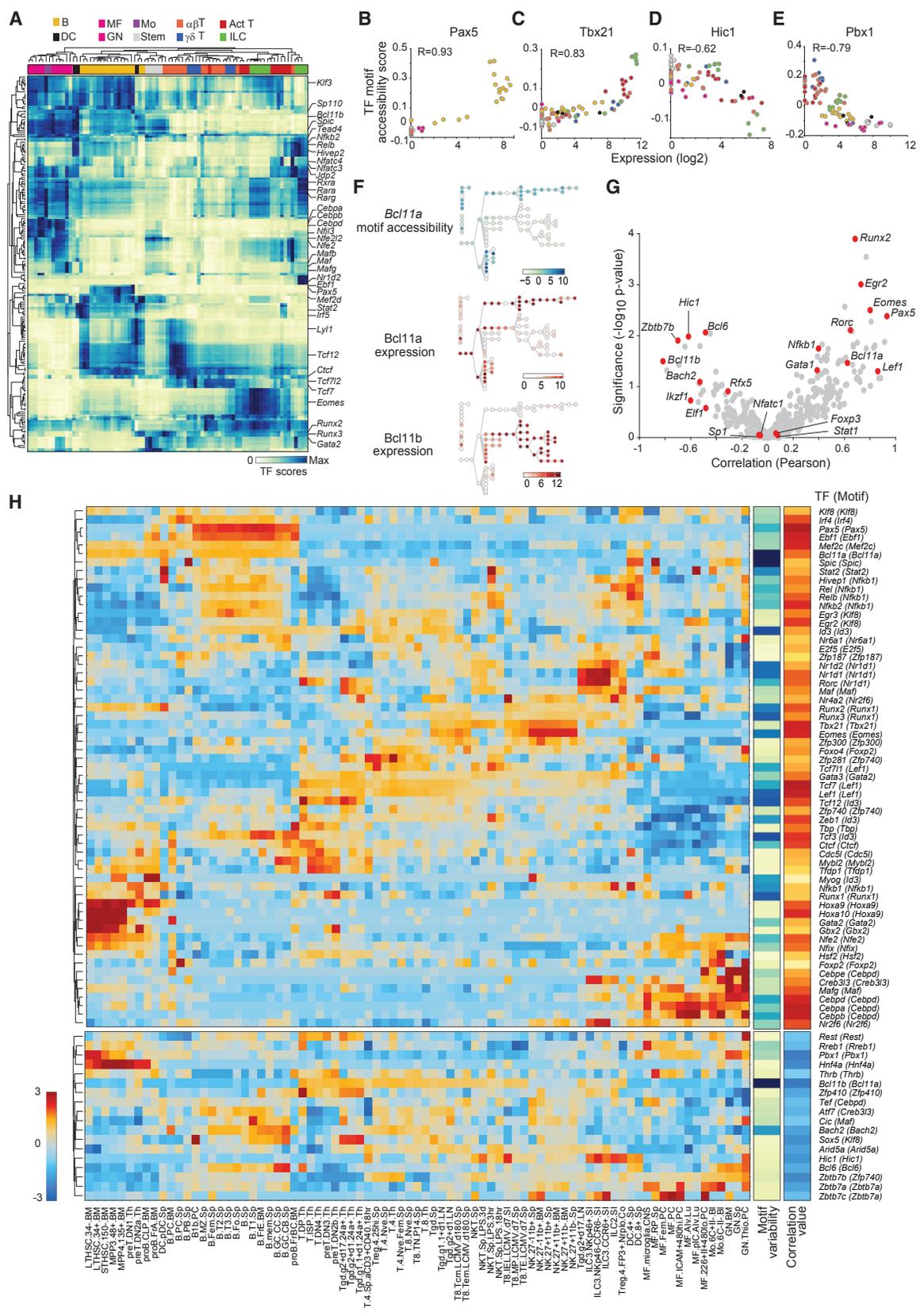
(legend on next page)

warrant further investigation: Bach1 in PC macrophages, Egr2 in alveolar macrophages, and Zeb1 in neutrophils. The motif for Ehf, a gene with expression restricted mostly to cDCs and epithelial cells (Figure S6A), was enriched in cDC-specific OCRs. This gene has roles in the regulation of inflammation and antigen transport in epithelial cells (Asai and Morrison, 2013; Fossum et al., 2017) and may have a similar function in cDCs.

CD4^{+} and CD8^{+} cDCs are developmentally and functionally related, yet have subtle but important differences in antigen presentation and in their transcriptomes (Miller et al., 2012). We identified several thousand differential OCRs between them, with dissimilar enrichments in some TF motifs (Figure 6C). The differentiation of CD8^{+} cDCs is dependent on Irf8 and Batf3 (Hildner et al., 2008; Tamura et al., 2005) and those motifs were correspondingly enriched in CD8^{+} DC OCRs. In contrast, CEBP family motifs were enriched in OCRs specific to CD4^{+} cDCs. Motifs enriched in CD103^{+}CD11b^{−} intestinal DCs, which are also Irf8-dependent (Ginhoux et al., 2009), were similar to those of CD8^{+} DCs (Figure S6B), including strong enrichments of transducers of type I interferon (IFN) signaling Stat2 and Irf9. The differential accessibility at steady-state of OCRs predicted to bind Stat2 and Irf9, suggests that Irf8-dependent cDCs may be specifically poised to respond to IFN-I. This type of signaling is specifically required by CD8^{+} and CD103^{+} DCs to promote cross presentation and an increased anti-viral state (Diamond et al., 2011; Helft et al., 2012).

TFs that Control OCR Dynamics during Lymphocyte Differentiation

We applied the same powerful logic as for Figure 5 of correlating the presence of a TF motif, the activity of the OCR, and the expression of the corresponding TF, to discover relevant sites of action for particular TFs in T and B lymphocyte differentiation. In Figure 7A, we plot the activity of OCRs with the best score for the RORγ-binding. Clustering these OCRs based on ATAC-seq intensity identified 6 patterns of OCR accessibility. Among those, one cluster (cl3) exhibited a clear relationship to the expression of *Rorc* gene in thymic DPs (Figure 7A; Table S7A) (p < 10^{−4}), and these OCRs coincided precisely with demonstrable RORγ binding from chromatin immunoprecipitation sequencing (ChIP-seq) data (Guo et al., 2016) (Figure 7A, right). Another cluster (cl4) seemed to respond to RORγ in colonic T regulatory (Treg) cells; some of the specific OCRs fall in close proximity with genes that are differentially expressed in RORγ[+] Tregs, such as *Il23r* (Table S7A). That different RORγ-binding OCRs are active in DP thymocytes and colonic RORγ[+] Tregs is consis-

tent with the notion that RORγ controls different transcriptional targets in a context-dependent manner (Sefik et al., 2015). The OCR clusters whose activity does not correlate with RORγ expression may correspond to false-positives from motif prediction or to TFs that share the same binding motif. To validate the prediction that cl3 represents OCRs whose accessibility depends on RORγ, we performed ATAC-seq in DPs from Rorc-deficient mice (*Rorc*[gfp/gfp]). Strikingly, almost all OCRs from the DP-specific cl3 disappeared in RORγ-deficient DPs (Figure 7B), while those of the uncorrelated cl6 were unaffected. Thus, RORγ seems to operate as a pioneer factor.

ThPOK (*Zbtb7b*) and Runx3 are key TFs for the branched differentiation of CD4^{+} and CD8^{+} T cells (Ellmeier and Taniuchi, 2014; Xiong and Bosselut, 2012). For Runx3, which is under dominant translation control, our approach would not be informative, but for ThPOK, the correlative approach proved highly suggestive: accessibility of many of the OCRs that contain its cognate motif was curtailed in T cells in which ThPOK was present (Figure 7C; Table S7B), especially those in cl2. This negative correlation (see also Figure 5G) is consistent with the dominant suppressive function of ThPOK, suggesting that it shuts down the CD8^{+} T lineage program not only by inhibiting Runx3 expression but also by directly inhibiting a swath of enhancer elements.

Together with EBF1, Pax5 is the major TF defining B lymphocyte identity, essential for both early development and to maintain the function of mature B cells (Horcher et al., 2001; Medvedovic et al., 2011). It is expressed throughout B cell differentiation before being silenced in plasma cells (Shi et al., 2015). Pax5's aggregated OCR scores directly correlate with its expression (Figure 5B, validated by prior ChIP-seq data) (Revilla-I-Domingo et al., 2012), but a clustered analysis of OCRs that contain its binding motif revealed a striking dynamic variation: OCRs in cl2 and cl3 became active at the proB.FrBC stage, only transiently for cl2, and more stably for cl3. OCRs of cl5 only became active later, in germinal center stages after immune activation, before being extinguished in plasma cells concomitant with the loss of expression (Figure 7D; Table S7C). These different behaviors of Pax5-binding OCRs are consistent with its context-specific activity (Revilla-I-Domingo et al., 2012).

FoxP3 is the key controller of Treg development and function (Ramsdell and Ziegler, 2014). It is not considered as a pioneer factor but binds and modifies active enhancer elements (Samstein et al., 2012). With the unique landscape available here, we revisited the status of FoxP3 binding sites across immunocyte differentiation. Among 2,000 high-confidence FoxP3-binding sites (Kitagawa et al., 2017; Kwon et al., 2017; Samstein et al., 2012), we identified 1,080 DE OCRs that were accessible

Figure 5. Regulators of Chromatin Accessibility
(A) Transcription factor motif accessibility scores, TFs in rows (z-normalized), and cell types in columns (hierarchically clustered).
(B–E) Relationship between the expression of (B) Pax5, (C) Tbx1, (D) Hic1, and (E) Pbx1 and its motif accessibility score for representative factors. Each point represents a cell type, color-coded per Figure 1A.
(F) Accessibility score of Bcl11a motifs (top; cells arranged per Figure 1A) in relation to the expression of Bcl11a or Bcl11b (bottom).
(G) Pearson coefficient and significance of correlations between TF motif score and TF expression (generalized from B–E). Known regulators of immune cell development and function are highlighted in red.
(H) Expression patterns of the TFs determined to significantly correlate with changes in chromatin accessibility (positive correlation, top block; negative, bottom). Side bars, motif variability and correlation coefficient.
See also Figure S5 and Tables S4 and S5.
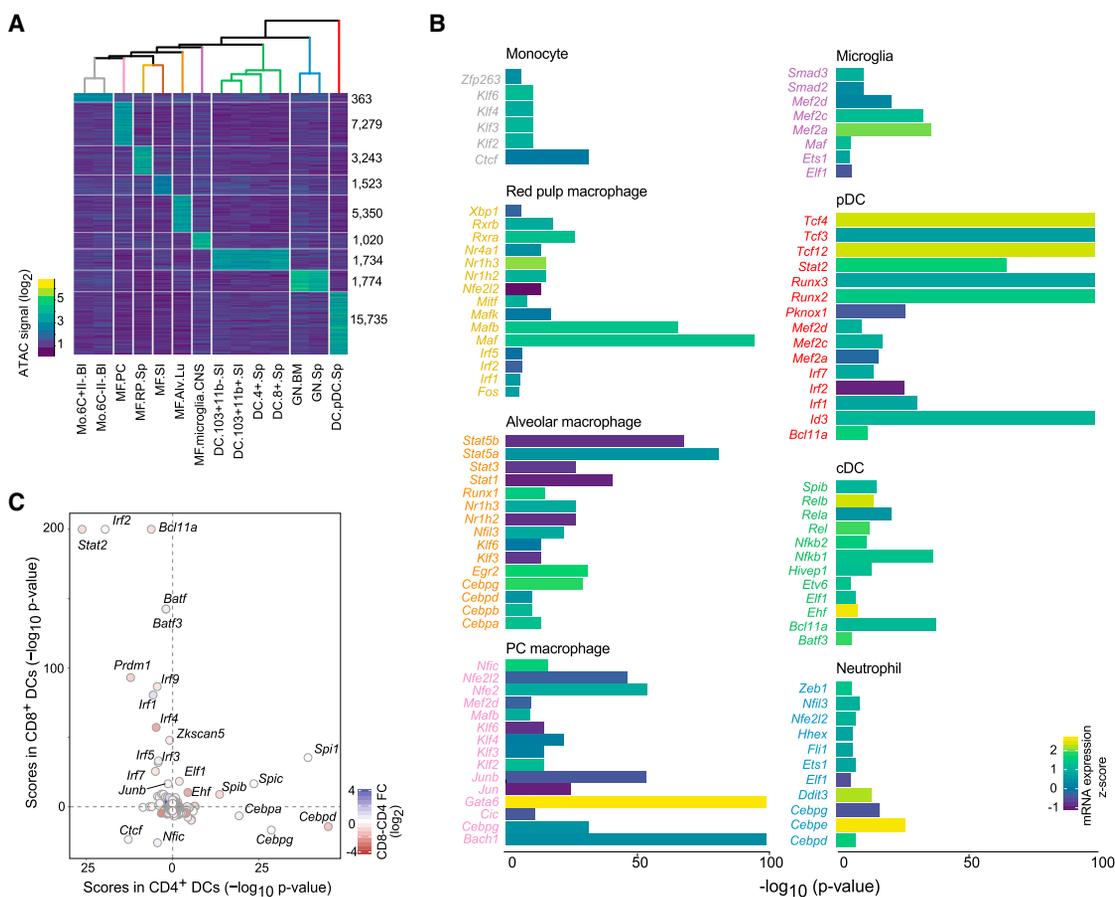
Figure 6. Regulatory Factors in Myeloid Cells Inferred from Chromatin Accessibility

(A) Differential OCR signals across all steady-state myeloid cells (right, numbers of distinguishing OCRs; top, correlation tree).

(B) TF motif enrichment scores (chromVAR z-test) in myeloid group-specific OCRs from (A), filtered for TF expression levels and statistical significance, with signed -log10 p values capped at 100 for display. Bars shaded by TF mRNA expression.

(C) Comparison of TF enrichment scores for OCRs accessible CD4+ and CD8+ cDCs, points are shaded according to the TF's mRNA expression fold change between the two DC subsets.

See also Figure S6 and Table S6.

in Tregs (Tables S7D and S7E). Consistent with prior conclusions (Samstein et al., 2012), many of these DE OCRs (80%) were constitutively accessible, from stem cells onward, and even in B or myeloid cells (Figure 7E); all FoxP3-binding OCRs that mapped to TSSs behaved similarly (Figure S7A). Another set of FoxP3-binding OCRs behaved more dynamically, only becoming active after the DP stage, suggesting control by thymic positive selection events. A small but distinct minority of these FoxP3-binding OCRs were Treg-specific (Figure 7E, right), suggesting that FoxP3 opens these regions, alone or with other Treg determining cofactors. Interestingly, the constitutive and dynamic OCR sets were markedly distinguished by their associated histone marks (Figure 7E, bottom) (data from Kitagawa et al., 2017). All were H3K27Ac-positive enhancer elements, but the active enhancer mark H3K4Me1 was much more prevalent among dynamic than constitutive OCRs (Figures 7E, bottom, and S7B). In addition, Nfkb(1/2)-binding motifs were specifically enriched in dynamic FoxP3 OCRs (Figure 7F),

consistent with the role of nuclear factor κB (NF-κB) family members in Treg differentiation (Oh et al., 2017). Ets and Lef1 binding sites were enriched in both classes on OCRs, while Forkhead or Runx motifs were preferentially present in constitutive FoxP3-binding OCRs. Thus, these analyses reveal the existence of two classes of FoxP3-binding enhancer elements. One is constitutively open in many immunocytes, while the other is activated with final Treg differentiation and seems to electively involve the NF-κB family of TFs. These examples highlight the power of these data to map OCRs that truly respond to a given TF and identify relevant binding sites (see http://immgen.org for a larger set of 300 TFs).

DISCUSSION

We profiled chromatin accessibility and gene expression in 90 cell types to generate a *cis*-regulatory atlas that encompasses the entire span of lineages that compose the mouse immune
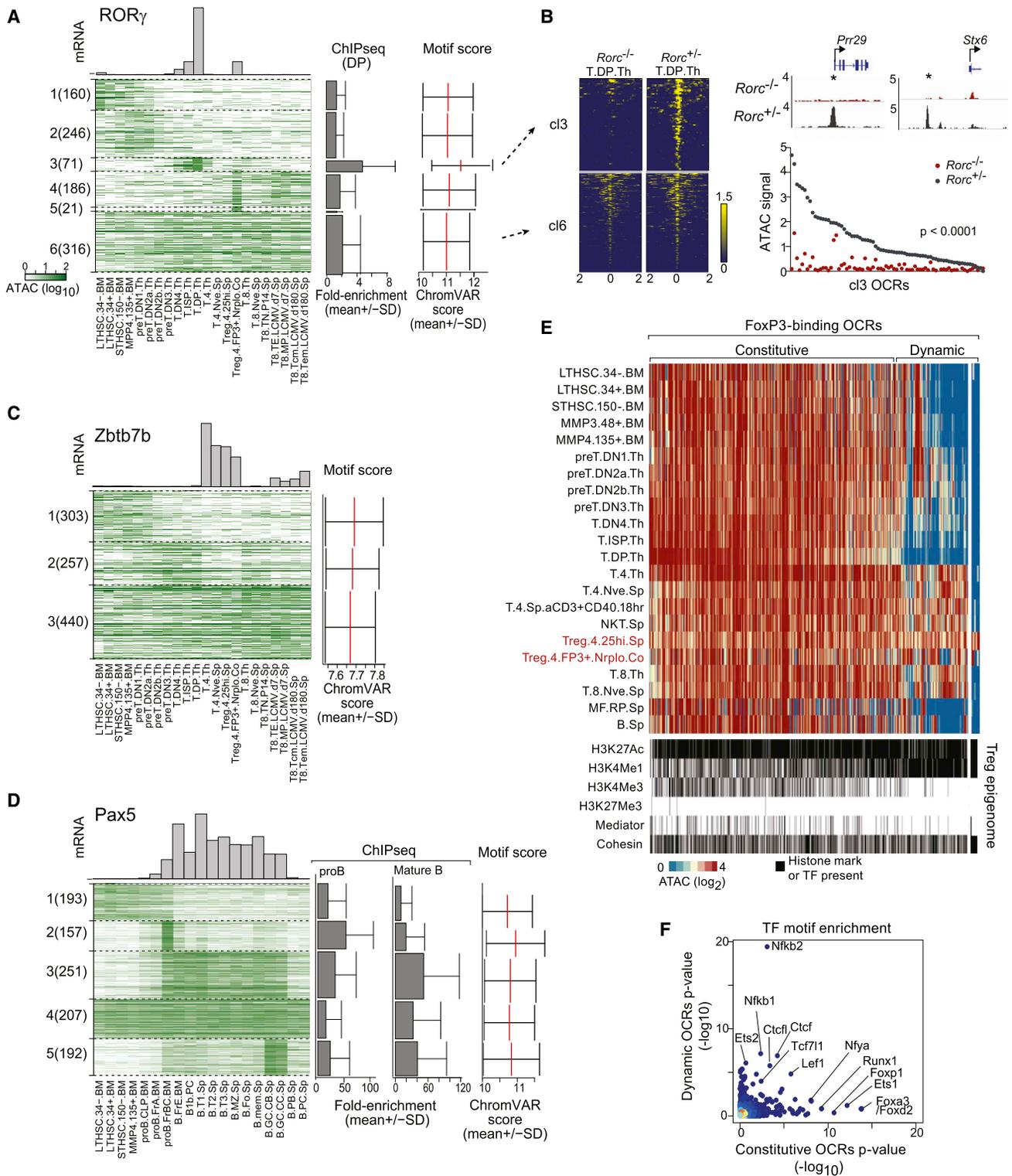
Figure 7. Dynamics of Chromatin Accessibilities on TF-Motif Containing OCRs along Differentiation

(A, C, and D) Cell type-dependent accessibility for OCRs that contain (A) RORγ, (B) Zbtb7b, or (D) Pax5 motifs (top 1,000 predicted OCRs, clustered by k-means. Top: mRNA levels. Right: TF motif scores and ChIP-seq signals averaged per cluster, ± SD).

(B) Normalized ATAC-seq intensity for OCRs that contain an RORγ-binding motif of cluster3 or cluster6 (from A), in immature DP thymocytes of *Rorc*-deficient mice or -positive littermates.

(legend continued on next page)

system. The paired chromatin and transcriptome approach, the focus on immunocytes, and the unprecedented granularity of the data enabled us to move beyond an epigenomic roadmap, providing a platform to infer causal regulatory interactions. Besides providing a deep resource of great value to understand immunological differentiation and function, the data bring insights of broad relevance on the role and positions of enhancer elements, reveal a deep dichotomy within mammalian gene regulation, and illuminate the relation between transcription factor activity and chromatin configuration.

Establishing this "complete" landscape of 512,595 *cis*-regulatory elements was enabled by sampling a large repertoire of closely related cell types, borderline significance of an ATAC peak in one cell type being bolstered by related cells. This fine mapping of cell state transitions enabled the analysis of regulatory interactions, which would not be possible with epigenomic data obtained from whole tissues, or from a partial sampling of specific cell types. We anticipate that future efforts with even finer parsing of some lineages, as well as single-cell approaches, may lead to an even more precise atlas. In the discussion and interpretation of the present data, we have assumed that OCRs distant from known TSS are likely to be enhancer elements. While some OCRs may correspond to other structures (e.g., TSS of unrecognized transcriptional units, or non-enhancer structural elements), the "rediscovery" of known enhancers in the vicinity of the *Cd4* and *Cd8* loci support the validity of this assumption.

We connected a number of OCRs to the expression of a nearby gene, based on the plausible assumption that such a correlation between accessibility of a *cis*-regulatory element and expression of a gene signifies a functional relationship. It has long been a conundrum to formally associate a *cis*-regulatory element with the gene(s) it might regulate. The "closest gene" is usually the default call, even though it is known that some enhancers can be effective from very long distances. The results of Figure 3C give some support to this general notion, by showing that genes are mostly associated with enhancers within 20 kb or less of their TSS. Indeed, the "closest gene" assignment is likely correct 90.2% of the time (from Table S3F). Widespread redundancy was another aspect of enhancer activity revealed by this analysis, as most genes with an enhancer correlated to their expression actually had several correlated enhancers (Figure 3D) which were themselves inter-connected. That enhancers are often repeated has been recognized from their first description (Banerji et al., 1981; Benoist and Chambon, 1981), and a recent study showed that 64% of *D. melanogaster* loci have redundant "shadow" enhancers (Cannavò et al., 2016). Redundancy may provide functional buffering and evolutionary flexibility and robustness (Hong et al., 2008; Osterwalder et al., 2018), or allow fine-tuning of a gene's transcription in slightly different stages or states, or be mechanistically more efficient, synergistic binding of the same TFs at closely spaced sites helping to stabilize an en-

hanceosome complex. Finally, we observed very few cases of silencer elements (defined as accessibility negatively correlated with expression of the target gene), suggesting that positive enhancement is the predominant mode of gene regulation in mammalian transcription.

We observed a striking partition between one set of genes whose activity seemed cued by the overall pattern of activity of all distal enhancers and another that was aligned to activity in promoter regions, with enrichment for different TFBS in the promoters of each class. There are precedents for such divergence. For instance, the housekeeping *Hprt* locus contains no discernible enhancer (Gasperini et al., 2017), and enhancer catalogs have generally shown them to be tissue-specific (Shen et al., 2012). This dichotomy may be related to the demonstration in *Drosophila* of enhancer-promoter specificities that distinguish housekeeping and differentiation-linked regulatory programs (Zabidi et al., 2015). More generally, it relates to the long-lasting debate on the differences between promoters and enhancers. Promoters are classically defined as sites that focus transcription initiation by recruiting Pol-II and basal transcription factors, while enhancers supercharge the promoters they target to increase the rate of transcription. But whether they truly represent different entities has been nuanced or challenged (Kim and Shiekhattar, 2015). The present results suggest that they do play fundamentally different roles in orchestrating transcription.

Beyond establishing the rich landscape of *cis*-regulatory regions, the three-way correlation between activity of an OCR, the TF motifs it contains, and the expression of the TFs allows for accurate and pointwise predictions of how TFs orchestrate immunocyte differentiation and function. We note that this approach is blind to some classes of TFs: opportunistic TFs that exploit already accessible chromatin regions (e.g., FoxP3), whose regulation is post-transcriptional, and those controlled by modification or localization (STATs, NF-AT). Our analyses accurately predicted TFs whose activity is associated with specific lineages and stages (Figure 5) and which specific OCRs (and genes) are actually activated by these TFs (Figures 7 and S7), this on an unprecedented scale. These include well-known TFs for which existing ChIP-seq data provide valuable validation and also TFs for which no such data were available (Gata2, Nfe2, or Eomes). Several of these profiles reveal a strong context dependence for TF action (e.g., for RORγ and Pax5) consistent with RORγ's different footprint in Th17 versus colonic Tregs (Sefik et al., 2015) and with Pax5's variable involvement along the B cell lineage (Revilla-I-Domingo et al., 2012), perhaps depend on cell-type specific post-translational modifications, co-factors, or ligands.

The analysis also reveals that TFs can have either positive or negative consequences on accessibility of an OCR. The former is readily conceptualized (docking of the factor displacing nucleosomes and/or recruiting additional chromatin modifiers), the

---

(E) Chromatin accessibility for 1,080 DE-OCRs known to bind FoxP3 in ChIP-seq experiments. Distal OCRs are classified as constitutive or dynamic (2-fold higher signal in Tregs than in precursor cell-types). ChIP-seq signal in these OCRs for mediator, cohesin, or histone marks in Tregs are shown below.
(F) TF motif enrichment score in constitutive and dynamic FoxP3-binding OCRs.
See also Figure S7 and Table S7.

latter less so, because closing of the element would potentially hinder the TF from binding. Some "hit-and-run" mechanism that instructs stable repressive histone marks or DNA methylation may be at play. It is generally thought that individual TFs can both activate or repress transcription, depending on local context. Our analyses (Figure 5G) suggest that many TFs dominantly play either activating or repressive roles (because dual function would result in no correlation overall). TFs with negative correlation between expression and motif accessibility include a Who's Who of known repressors (Pbx1, Bcl11b, Zbtb7b). A majority of TFs, however, had positive effects on accessibility, prompting the speculation that opening of chromatin is the dominant mode of control for the unfolding of gene expression through immune cell differentiation. This conclusion is consistent with observations that target activation by Pax5 and PU.1 correlated positively with DNA binding (Champhekar et al., 2015; Revilla-I-Domingo et al., 2012). Mechanistically, PU.1 has recently been shown to indirectly repress genes in T cell progenitors via TF theft, recruiting partner TFs to its own directly activated genes and thus depleting them from their own targets (Hosokawa et al., 2018).

In conclusion, this resource provides an atlas of *cis*-regulatory elements that will be leveraged by the community to guide focused experiments to understand the regulation of a particular locus through immune function or disease. This *cis*-regulatory atlas may serve as an initial scaffold on which to systematically build, through complementary "multi-omics" strategies, additional knowledge toward a complete understanding of genomic regulation in immune cells.

STAR★METHODS

Detailed methods are provided in the online version of this paper and include the following:

- KEY RESOURCES TABLE
- CONTACT FOR REAGENT AND RESOURCE SHARING
- EXPERIMENTAL MODEL AND SUBJECT DETAILS
  - Mice
- METHOD DETAILS
  - ATAC-seq Data Generation
  - ATAC-seq Quantification and Normalization
  - ATAC-seq QC
  - RNA-seq
- QUANTIFICATION AND STATISTICAL ANALYSIS
  - Dimensionality Reduction and Visualization with t-SNE
  - OCR Variance Component Analysis
  - Associating OCRs with Target Genes
  - Computing Aggregated OCR Scores
  - Annotating OCRs with motifs
  - Associating Aggregated Motif Scores with Transcription Factor Expression
  - Motif Enrichment in TSS
  - Analysis of Myeloid Lineage
  - Analysis of T Lineage
  - FoxP3 Analysis
- DATA AND SOFTWARE AVAILABILITY
  - Additional resources

REFERENCES

Anscombe, F.J. (1948). The transformation of Poisson, binomial and negative-binomial data. Biometrika *35*, 246–254.

Asai, T., and Morrison, S.L. (2013). The SRC family tyrosine kinase HCK and the ETS family transcription factors SPIB and EHF regulate transcytosis across a human follicle-associated epithelium model. J. Biol. Chem. *288*, 10395–10405.

Bahr, C., von Paleske, L., Uslu, V.V., Remeseiro, S., Takayama, N., Ng, S.W., Murison, A., Langenfeld, K., Petretich, M., Scognamiglio, R., et al. (2018). A Myc enhancer cluster regulates normal and leukaemic haematopoietic stem cell hierarchies. Nature *553*, 515–520.

Banerji, J., Rusconi, S., and Schaffner, W. (1981). Expression of a beta-globin gene is enhanced by remote SV40 DNA sequences. Cell *27*, 299–308.

Benoist, C., and Chambon, P. (1981). In vivo sequence requirements of the SV40 early promotor region. Nature *290*, 304–310.

Bornstein, C., Winter, D., Barnett-Itzhaki, Z., David, E., Kadri, S., Garber, M., and Amit, I. (2014). A negative feedback loop of transcription factors specifies alternative dendritic cell chromatin states. Mol. Cell *56*, 749–762.

Buenrostro, J.D., Giresi, P.G., Zaba, L.C., Chang, H.Y., and Greenleaf, W.J. (2013). Transposition of native chromatin for fast and sensitive epigenomic profiling of open chromatin, DNA-binding proteins and nucleosome position. Nat. Methods *10*, 1213–1218.

Buenrostro, J.D., Wu, B., Litzenburger, U., Gonzales, M., Ruff, D., Snyder, M., Chang, H.Y., and Greenleaf, W.J. (2015). Single-cell chromatin accessibility reveals principles of regulatory variation. Nature *523*, 486–490.

Cannavò, E., Khoueiry, P., Garfield, D.A., Geeleher, P., Zichner, T., Gustafson, E.H., Ciglar, L., Korbel, J.O., and Furlong, E.E.M. (2016). Shadow enhancers are pervasive features of developmental regulatory networks. Curr. Biol. *26*, 38–51.

Champhekar, A., Damle, S.S., Freedman, G., Carotta, S., Nutt, S.L., and Rothenberg, E.V. (2015). Regulation of early T-lineage gene expression and developmental progression by the progenitor cell transcription factor PU.1. Genes Dev. *29*, 832–848.

Chen, L., Ge, B., Casale, F.P., Vasquez, L., Kwan, T., Garrido-Martín, D., Watt, S., Yan, Y., Kundu, K., Ecker, S., et al. (2016). Genetic drivers of epigenetic and transcriptional variation in human immune cells. Cell 167, 1398–1414.

Cisse, B., Caton, M.L., Lehner, M., Maeda, T., Scheu, S., Locksley, R., Holmberg, D., Zweier, C., den Hollander, N.S., Kant, S.G., et al. (2008). Transcription factor E2-2 is an essential and specific regulator of plasmacytoid dendritic cell development. Cell 135, 37–48.

Corces, M.R., Buenrostro, J.D., Wu, B., Greenside, P.G., Chan, S.M., Koenig, J.L., Snyder, M.P., Pritchard, J.K., Kundaje, A., Greenleaf, W.J., et al. (2016). Lineage-specific and single-cell chromatin accessibility charts human hematopoiesis and leukemia evolution. Nat. Genet. 48, 1193–1203.

Deczkowska, A., Matcovitch-Natan, O., Tsitsou-Kampeli, A., Ben-Hamo, S., Dvir-Szternfeld, R., Spinrad, A., Singer, O., David, E., Winter, D.R., Smith, L.K., et al. (2017). Mef2C restrains microglial inflammatory response and is lost in brain ageing in an IFN-I-dependent manner. Nat. Commun. 8, 717.

Delogu, A., Schebesta, A., Sun, Q., Aschenbrenner, K., Perlot, T., and Busslinger, M. (2006). Gene repression by Pax5 in B cells is essential for blood cell homeostasis and is reversed in plasma cells. Immunity 24, 269–281.

Diamond, M.S., Kinder, M., Matsushita, H., Mashayekhi, M., Dunn, G.P., Archambault, J.M., Lee, H., Arthur, C.D., White, J.M., Kalinke, U., et al. (2011). Type I interferon is selectively required by dendritic cells for immune rejection of tumors. J. Exp. Med. 208, 1989–2003.

Dixon, J.R., Gorkin, D.U., and Ren, B. (2016). Chromatin domains: the unit of chromosome organization. Mol. Cell 62, 668–680.

Ellmeier, W., and Taniuchi, I. (2014). The role of BTB-zinc finger transcription factors during T cell development and in the regulation of T cell-mediated immunity. Curr. Top. Microbiol. Immunol. 381, 21–49.

ENCODE Project Consortium (2012). An integrated encyclopedia of DNA elements in the human genome. Nature 489, 57–74.

Ficara, F., Murphy, M.J., Lin, M., and Cleary, M.L. (2008). Pbx1 regulates self-renewal of long-term hematopoietic stem cells by maintaining their quiescence. Cell Stem Cell 2, 484–496.

Fossum, S.L., Mutolo, M.J., Tugores, A., Ghosh, S., Randell, S.H., Jones, L.C., Leir, S.-H., and Harris, A. (2017). Ets homologous factor (EHF) has critical roles in epithelial dysfunction in airway disease. J. Biol. Chem. 292, 10938–10949.

Gasperini, M., Findlay, G.M., McKenna, A., Milbank, J.H., Lee, C., Zhang, M.D., Cusanovich, D.A., and Shendure, J. (2017). CRISPR/Cas9-mediated scanning for regulatory elements required for HPRT1 expression via thousands of large, programmed genomic deletions. Am. J. Hum. Genet. 101, 192–205.

Ginhoux, F., Liu, K., Helft, J., Bogunovic, M., Greter, M., Hashimoto, D., Price, J., Yin, N., Bromberg, J., Lira, S.A., et al. (2009). The origin and development of nonlymphoid tissue CD103+ DCs. J. Exp. Med. 206, 3115–3130.

Guilliams, M., Ginhoux, F., Jakubzick, C., Naik, S.H., Onai, N., Schraml, B.U., Segura, E., Tussiwand, R., and Yona, S. (2014). Dendritic cells, monocytes and macrophages: a unified nomenclature based on ontogeny. Nat. Rev. Immunol. 14, 571–578.

Guo, Y., MacIsaac, K.D., Chen, Y., Miller, R.J., Jain, R., Joyce-Shaikh, B., Ferguson, H., Wang, I.-M., Cristescu, R., Mudgett, J., et al. (2016). Inhibition of RORγT skews TCRα gene rearrangement and limits T cell repertoire diversity. Cell Rep. 17, 3206–3218.

Hardy, R.R., and Hayakawa, K. (2001). B cell development pathways. Annu. Rev. Immunol. 19, 595–621.

Helft, J., Manicassamy, B., Guermonprez, P., Hashimoto, D., Silvin, A., Agudo, J., Brown, B.D., Schmolke, M., Miller, J.C., Leboeuf, M., et al. (2012). Cross-presenting CD103+ dendritic cells are protected from influenza virus infection. J. Clin. Invest. 122, 4037–4047.

Hildner, K., Edelson, B.T., Purtha, W.E., Diamond, M., Matsushita, H., Kohyama, M., Calderon, B., Schraml, B.U., Unanue, E.R., Diamond, M.S., et al. (2008). Batf3 deficiency reveals a critical role for CD8alpha+ dendritic cells in cytotoxic T cell immunity. Science 322, 1097–1100.

Hnisz, D., Day, D.S., and Young, R.A. (2016). Insulated neighborhoods: structural and functional units of mammalian gene control. Cell 167, 1188–1200.

Hong, J.-W., Hendrix, D.A., and Levine, M.S. (2008). Shadow enhancers as a source of evolutionary novelty. Science 321, 1314.

Horcher, M., Souabni, A., and Busslinger, M. (2001). Pax5/BSAP maintains the identity of B cells in late B lymphopoiesis. Immunity 14, 779–790.

Hosokawa, H., Ungerbäck, J., Wang, X., Matsumoto, M., Nakayama, K.I., Cohen, S.M., Tanaka, T., and Rothenberg, E.V. (2018). Transcription factor PU.1 represses and activates gene expression in early T cells by redirecting partner transcription factor binding. Immunity 48, 1119–1134.

Issuree, P.D.A., Ng, C.P., and Littman, D.R. (2017). Heritable gene regulation in the CD4:CD8 T cell lineage choice. Front. Immunol. 8, 291.

Kim, T.-K., and Shiekhattar, R. (2015). Architectural and functional commonalities between enhancers and promoters. Cell 162, 948–959.

Kitagawa, Y., Ohkura, N., Kidani, Y., Vandenbon, A., Hirota, K., Kawakami, R., Yasuda, K., Motooka, D., Nakamura, S., Kondo, M., et al. (2017). Guidance of regulatory T cell development by Satb1-dependent super-enhancer establishment. Nat. Immunol. 18, 173–183.

Kwon, H.-K., Chen, H.-M., Mathis, D., and Benoist, C. (2017). Different molecular complexes that mediate transcriptional induction and repression by FoxP3. Nat. Immunol. 18, 1238–1248.

Lara-Astiaso, D., Weiner, A., Lorenzo-Vivas, E., Zaretsky, I., Jaitin, D.A., David, E., Keren-Shaul, H., Mildner, A., Winter, D., Jung, S., et al. (2014). Immunogenetics. Chromatin state dynamics during blood formation. Science 345, 943–949.

Lavin, Y., Winter, D., Blecher-Gonen, R., David, E., Keren-Shaul, H., Merad, M., Jung, S., and Amit, I. (2014). Tissue-resident macrophage enhancer landscapes are shaped by the local microenvironment. Cell 159, 1312–1326.

Medvedovic, J., Ebert, A., Tagoh, H., and Busslinger, M. (2011). Pax5: a master regulator of B cell development and leukemogenesis. Adv. Immunol. 111, 179–206.

Mercer, E.M., Lin, Y.C., Benner, C., Jhunjhunwala, S., Dutkowski, J., Flores, M., Sigvardsson, M., Ideker, T., Glass, C.K., and Murre, C. (2011). Multilineage priming of enhancer repertoires precedes commitment to the B and myeloid cell lineages in hematopoietic progenitors. Immunity 35, 413–425.

Miller, J.C., Brown, B.D., Shay, T., Gautier, E.L., Jojic, V., Cohain, A., Pandey, G., Leboeuf, M., Elpek, K.G., Helft, J., et al.; Immunological Genome Consortium (2012). Deciphering the transcriptional network of the dendritic cell lineage. Nat. Immunol. 13, 888–899.

Oh, H., Grinberg-Bleyer, Y., Liao, W., Maloney, D., Wang, P., Wu, Z., Wang, J., Bhatt, D.M., Heise, N., Schmid, R.M., et al. (2017). An NF-κB transcription-factor-dependent lineage-specific transcriptional program promotes regulatory T cell identity and function. Immunity 47, 450–465.

Osterwalder, M., Barozzi, I., Tissières, V., Fukuda-Yuzawa, Y., Mannion, B.J., Afzal, S.Y., Lee, E.A., Zhu, Y., Plajzer-Frick, I., Pickle, C.S., et al. (2018). Enhancer redundancy provides phenotypic robustness in mammalian development. Nature 554, 239–243.

Picelli, S., Faridani, O.R., Björklund, A.K., Winberg, G., Sagasser, S., and Sandberg, R. (2014). Full-length RNA-seq from single cells using Smart-seq2. Nat. Protoc. 9, 171–181.

Placek, K., Hu, G., Cui, K., Zhang, D., Ding, Y., Lee, J.-E., Jang, Y., Wang, C., Konkel, J.E., Song, J., et al. (2017). MLL4 prepares the enhancer landscape for Foxp3 induction via chromatin looping. Nat. Immunol. 18, 1035–1045.

Quinlan, A.R., and Hall, I.M. (2010). BEDTools: a flexible suite of utilities for comparing genomic features. Bioinformatics 26, 841–842.

Ramsdell, F., and Ziegler, S.F. (2014). FOXP3 and scurfy: how it all began. Nat. Rev. Immunol. 14, 343–349.

Reizis, B., Bunin, A., Ghosh, H.S., Lewis, K.L., and Sisirak, V. (2011). Plasmacytoid dendritic cells: recent progress and open questions. Annu. Rev. Immunol. 29, 163–183.

Revilla-I-Domingo, R., Bilic, I., Vilagos, B., Tagoh, H., Ebert, A., Tamir, I.M., Smeenk, L., Trupke, J., Sommer, A., Jaritz, M., and Busslinger, M. (2012). The B-cell identity factor Pax5 regulates distinct transcriptional programmes in early and late B lymphopoiesis. EMBO J. 31, 3130–3146.

Roadmap Epigenomics Consortium, Kundaje, A., Meuleman, W., Ernst, J., Bilenky, M., Yen, A., Heravi-Moussavi, A., Kheradpour, P., Zhang, Z., Wang, J., et al. (2015). Integrative analysis of 111 reference human epigenomes. Nature *518*, 317–330.

Rosas, M., Davies, L.C., Giles, P.J., Liao, C.-T., Kharfan, B., Stone, T.C., O'Donnell, V.B., Fraser, D.J., Jones, S.A., and Taylor, P.R. (2014). The transcription factor Gata6 links tissue macrophage phenotype and proliferative renewal. Science *344*, 645–648.

Rothenberg, E.V. (2014). Transcriptional control of early T and B cell developmental choices. Annu. Rev. Immunol. *32*, 283–321.

Samstein, R.M., Arvey, A., Josefowicz, S.Z., Peng, X., Reynolds, A., Sandstrom, R., Neph, S., Sabo, P., Kim, J.M., Liao, W., et al. (2012). Foxp3 exploits a pre-existent enhancer landscape for regulatory T cell lineage specification. Cell *151*, 153–166.

Schep, A.N., Wu, B., Buenrostro, J.D., and Greenleaf, W.J. (2017). chromVAR: inferring transcription-factor-associated accessibility from single-cell epigenomic data. Nat. Methods *14*, 975–978.

Sefik, E., Geva-Zatorsky, N., Oh, S., Konnikova, L., Zemmour, D., McGuire, A.M., Burzyn, D., Ortiz-Lopez, A., Lobera, M., Yang, J., et al. (2015). MUCOSAL IMMUNOLOGY. Individual intestinal symbionts induce a distinct population of RORγ⁺ regulatory T cells. Science *349*, 993–997.

Shen, Y., Yue, F., McCleary, D.F., Ye, Z., Edsall, L., Kuan, S., Wagner, U., Dixon, J., Lee, L., Lobanenkov, V.V., and Ren, B. (2012). A map of the cis-regulatory sequences in the mouse genome. Nature *488*, 116–120.

Shi, W., Liao, Y., Willis, S.N., Taubenheim, N., Inouye, M., Tarlinton, D.M., Smyth, G.K., Hodgkin, P.D., Nutt, S.L., and Corcoran, L.M. (2015). Transcriptional profiling of mouse B cell terminal differentiation defines a signature for antibody-secreting plasma cells. Nat. Immunol. *16*, 663–673.

Tamura, T., Tailor, P., Yamaoka, K., Kong, H.J., Tsujimura, H., O'Shea, J.J., Singh, H., and Ozato, K. (2005). IFN regulatory factor-4 and -8 govern dendritic cell subset development and their functional diversity. J. Immunol. *174*, 2573–2581.

Wang, L., Wildt, K.F., Castro, E., Xiong, Y., Feigenbaum, L., Tessarollo, L., and Bosselut, R. (2008). The zinc finger transcription factor Zbtb7b represses CD8-lineage gene expression in peripheral CD4+ T cells. Immunity *29*, 876–887.

Xiong, Y., and Bosselut, R. (2012). CD4-CD8 differentiation in the thymus: connecting circuits and building memories. Curr. Opin. Immunol. *24*, 139–145.

Ye, C.J., Feng, T., Kwon, H.-K., Raj, T., Wilson, M.T., Asinovski, N., McCabe, C., Lee, M.H., Frohlich, I., Paik, H.-I., et al. (2014). Intersection of population variation and autoimmunity genetics in human T cell activation. Science *345*, 1254665.

Yu, B., Zhang, K., Milner, J.J., Toma, C., Chen, R., Scott-Browne, J.P., Pereira, R.M., Crotty, S., Chang, J.T., Pipkin, M.E., et al. (2017). Epigenetic landscapes reveal transcription factors that regulate CD8⁺ T cell differentiation. Nat. Immunol. *18*, 573–582.

Yui, M.A., and Rothenberg, E.V. (2014). Developmental gene networks: a triathlon on the course to T cell identity. Nat. Rev. Immunol. *14*, 529–545.

Zabidi, M.A., Arnold, C.D., Schernhuber, K., Pagani, M., Rath, M., Frank, O., and Stark, A. (2015). Enhancer-core-promoter specificity separates developmental and housekeeping gene regulation. Nature *518*, 556–559.

STAR★METHODS

KEY RESOURCES TABLE

REAGENT or RESOURCE	SOURCE	IDENTIFIER
Antibodies		
CD4 APC	Thermo Fisher Scientific	clone: RM4-5; cat#: 17-0042-81; lab: Brown
MHC II APC-eFluor780	Thermo Fisher Scientific	clone: M5/114.15.2; cat#: 47-5321-82; lab: Brown
CD45 APC-eFluor780	Thermo Fisher Scientific	clone: 30-F11m; cat#: 47-0451-82; lab: Brown
CD11c PE-Cy7	Thermo Fisher Scientific	clone: N418; cat#: 25-0114-82; lab: Brown
MHC II eFluor450	Thermo Fisher Scientific	clone: M5/114.15.2; cat#: 48-5321-82; lab: Brown
CD103 PE	Thermo Fisher Scientific	clone: 2E7; cat#: 12-1031-82; lab: Brown
CD64 APC	Thermo Fisher Scientific	clone: X54-5/7.1; cat#: 17-0641-82; lab: Brown
CD11b FITC	Thermo Fisher Scientific	clone: M1/70; cat#: 11-0112-82; lab: Brown
Siglec F PE	Thermo Fisher Scientific	clone: 1RNM44N; cat#: 12-1702-82; lab: Brown
CD11c PE-Cy7	Thermo Fisher Scientific	clone: N418; cat#: 25-0114-82; lab: Brown
CD45 BV510	BD Biosciences	clone: 30-F11; cat#: 563891; lab: Brown
CD8 PE	Thermo Fisher Scientific	clone: 53-6.7; cat#: 12-0081-82; lab: Brown
CD3 FITC	Thermo Fisher Scientific	clone: eBio500A2; cat#: 11-0033-82; lab: Brown
CD19 FITC	Thermo Fisher Scientific	clone: eBio1D3; cat#: 11-0193-82; lab: Brown
CD11c PE	Thermo Fisher Scientific	clone: N418; cat#: MA5-16878; lab: Brown
B220 eFluor450	Thermo Fisher Scientific	clone: RA3-6B2; cat#: 48-0452-82; lab: Brown
PDCA1 APC	Thermo Fisher Scientific	clone: eBio927; cat#: 17-3172-82; lab: Brown
Siglec H PE-Cy7	Thermo Fisher Scientific	clone: eBio440c; cat#: 25-0333-82; lab: Brown
cd45 PE-Cy7	Biolegend	clone: 30F11; cat#: 103114; lab: Turley
Epcam PE-Cy7	Biolegend	clone: G8.8; cat#: 118216; lab: Turley
Ter11 PE-Cy7	Biolegend	clone: TER119; cat#: 116222; lab: Turley
CD21/35 FITC	Biolegend	clone: 7E9; cat#: 123407; lab: Turley
Madcam 488	Biolegend	clone: MECA-367; cat#: 120708; lab: Turley
PDPN APC	Biolegend	clone: 8.1.1; cat#: 127410; lab: Turley
CD140a PE	BD PharMingen	clone: APA5; cat#: 562776; lab: Turley
CD31 PE-Dazzle	Biolegend	clone: 390; cat#: 102430; lab: Turley
Calcein Blue	Molecular Probes	clone: NA; cat#: C1429; lab: Turley
Live/Dead Near-IR633	Molecular Probes	clone: NA; cat#: L10119; lab: Turley
CD45.2 FITC	Invitrogen	clone: 104; cat#: 11-0454-85; lab: Goldrath
CD127 PE-Cy7	Invitrogen	clone: A7R34; cat#: 25-1271-82; lab: Goldrath
CD8a APC-eFluor780	Invitrogen	clone: GK1.5; cat#: 47-0041-82; lab: Goldrath
CD45.1 APC	Invitrogen	clone: A20; cat#: 17-0453-82; lab: Goldrath

(Continued on next page)

Continued

REAGENT or RESOURCE	SOURCE	IDENTIFIER
KLRG1 E450	Invitrogen	clone: 2F1; cat#: 48-5893-82; lab: Goldrath
CD44 PE-Cy7	Invitrogen	clone: IM7; cat#: 25-0441-82; lab: Goldrath
CD62L APC	BioLegend	clone: MEL-14; cat#: 104412; lab: Goldrath
Rat anti-mouse CD4 PE-Cy7	BD Biosciences	clone: RM4-5; cat#: 552775; lab: Kang
Rat anti-mouse CD8a PE-Cy7	BD Biosciences	clone: 53-6.7; cat#: 552877; lab: Kang
Hamster anti-mouse CD3e PerCP-Cy5.5	BD Biosciences	clone: 145-2C11; cat#: 551163; lab: Kang
Hamster anti-mouse TCRd BV 421	Biolegend	clone: GL3; cat#: 118120; lab: Kang
Hamster anti-mouse Vg2-FITC	Biolegend	clone: UC3-10A6; cat#: 137703; lab: Kang
Hamster anti-mouse Vg1.1-APC	Biolegend	clone: 2.11; cat#: 141108; lab: Kang
Rat anti-mouse CD24 APC-eFluor780	eBioscience	clone: M1/69; cat#: 48-0242-82; lab: Kang
Rat anti-mouse Scart2	J. Kisielow	clone: NA; cat#: NA; lab: Kang
Hamster anti-mouse CD27 PE	eBioscience	clone: LG.7F9; cat#: 12-0271-81; lab: Kang
CD19	eBioscience	clone: MB19-1; cat#: NA; lab: Edy Kim
Ter119	eBioscience	clone: TER119; cat#: NA; lab: Edy Kim
Ly6G/Gr1	eBioscience	clone: A18; cat#: NA; lab: Edy Kim
CD8α	eBioscience	clone: 53/6.7; cat#: NA; lab: Edy Kim
TCRβ	eBioscience	clone: H58-597; cat#: NA; lab: Edy Kim
mCD1d tetramer PBS-57 APC	NIH Tetramer Core Facility	clone: NA; cat#: NA; lab: Edy Kim
CD3 FITC	eBioscience	clone: eBio500A2; cat#: 11-0033-82; lab: Merad
CD19 FITC	eBioscience	clone: eBio1D3; cat#: 11-0193-82; lab: Merad
CD8 PE	BioLegend	clone: 53-6.7; cat#: 100707; lab: Merad
CD4 APC	BioLegend	clone: GK1.5; cat#: 100411; lab: Merad
CD11c PE/Cy7	BioLegend	clone: N418; cat#: 117317; lab: Merad
CD45 BV510	BioLegend	clone: 30-F11; cat#: 103137; lab: Merad
MHCII APC/Cy7	BioLegend	clone: M5/114.15.2; cat#: 107627; lab: Merad
PDCA1 APC	eBioscience	clone: ebio927; cat#: 17-3172-82; lab: Merad
B220 eF450	BioLegend	clone: RA3-6B2; cat#: 103239; lab: Merad
Siglec H Pe/Cy7	eBioscience	clone: ebio440c; cat#: 25-0333-82; lab: Merad
CD64 APC	BioLegend	clone: X54-5/7.1; cat#: 139305; lab: Merad
CD103 PE	BioLegend	clone: 2E7; cat#: 121405; lab: Merad
CD11b FITC	BioLegend	clone: M1/70; cat#: 101205; lab: Merad
Siglec F PE	BD Biosciences	clone: E50-2440; cat#: 552126; lab: Merad
CD4	UCSF Ab core	clone: GK1.5; cat#: AM012; lab: Nabekura
CD5	UCSF Ab core	clone: 53-7.3; cat#: AM018; lab: Nabekura
CD8a	UCSF Ab core	clone: 2.43; cat#: AM023; lab: Nabekura
CD19	UCSF Ab core	clone: 1D3; cat#: AM005; lab: Nabekura
Gr-1	UCSF Ab core	clone: RB6-8C5; cat#: AM051; lab: Nabekura
Ter110	UCSF Ab core	clone: Ter119; cat#: AM030; lab: Nabekura
BioMag goat anti-rat IgG beads	QIAGEN	clone: NA; cat#: 310107; lab: Nabekura
CD49b FITC	BioLegend	clone: DX5; cat#: 108906; lab: Nabekura
NK1.1 PerCP-Cy5.5	BioLegend	clone: PK136; cat#: 108728; lab: Nabekura

Continued

REAGENT or RESOURCE	SOURCE	IDENTIFIER
CD3e PE-CY7	BioLegend	clone: 145-2C11; cat#: 100320; lab: Nabekura
CD19 PE-CY7	BD Biosciences	clone: 1D3; cat#: 552854; lab: Nabekura
CD11b PE	BD Biosciences	clone: M1/70; cat#: 553311; lab: Nabekura
CD27 APC	BioLegend	clone: LG.3A10; cat#: 124212; lab: Nabekura
CD49a Biotin	Miltenyi Biotec	clone: REA493; cat#: 130-107-587; lab: Nabekura
CD127 Biotin	BioLegend	clone: A7R34; cat#: 135006; lab: Nabekura
CD51 Biotin	BD Biosciences	clone: RMV-7; cat#: 551380; lab: Nabekura
Streptavidin-BV421	BioLegend	clone: NA; cat#: 405226; lab: Nabekura
Propidium Iodide	Sigma-Aldrich	clone: NA; cat#: P4170; lab: Nabekura
CD138 PECy7	BioLegend	clone: 281-2; cat#: 142514; lab: Nutt
CD138 PE	BDBiosciences	clone: 281-2; cat#: 553714; lab: Nutt
CD38 Alexa fluor 680	in house	clone: 90; cat#: NA; lab: Nutt
NK1.1 APC	BD Biosciences	clone: PK136; cat#: 550627; lab: Nutt
CD11b (MAC-1) Alexa fluor 647	in house	clone: M1/70; cat#: NA; lab: Nutt
TCRb APC	eBioscience	clone: H57-597; cat#: 17-5961-83; lab: Nutt
TCRb PE	BD Biosciences	clone: H57-597; cat#: 553172; lab: Nutt
MHC-II APC-eFluor780	eBioscience	clone: M5/114.15.2; cat#: 47-5321-82; lab: Nutt
Gr-1 (Ly-6G) PE	in house	clone: RB6-8C5; cat#: NA; lab: Nutt
B220 (CD45R) FITC	in house	clone: RA3-6B2; cat#: NA; lab: Nutt
CD95 (Fas) PECy7	BD Biosciences	clone: Jo2; cat#: 557653; lab: Nutt
CXCR4 BV421	BD Biosciences	clone: 2B11; cat#: 585522; lab: Nutt
CD86 BV605	BD Biosciences	clone: GL1; cat#: 563055; lab: Nutt
IgM APC-eFluor780	eBioscience	clone: II/41; cat#: 47-5790-82; lab: Nutt
IgD APC-eFluor780	eBioscience	clone: 11-26C; cat#: 47-5993-80; lab: Nutt
IgG BV421	BioLegend	clone: Poly4053; cat#: 405317; lab: Nutt
CD117 PE-Cy7	BioLegend	clone: 2B8; cat#: 105814; lab: Benoist
CD11b PerCPcy5.5	BioLegend	clone: M1/70; cat#: 101228; lab: Benoist
CD11b PE	BioLegend	clone: M1/70; cat#: 101208; lab: Benoist
CD11C A700	BioLegend	clone: N418; cat#: 117320; lab: Benoist
CD11c APC-Cy7	BioLegend	clone: N418; cat#: 117324; lab: Benoist
CD19 APC-ef780	eBiosciences	clone: 1D3; cat#: 47-0193-82; lab: Benoist
CD19 PE-TR	eBiosciences	clone: 1D3; cat#: 61-0193-82; lab: Benoist
CD19 PE-Cy7	BioLegend	clone: 1D3; cat#: 115520; lab: Benoist
CD19 APC-Cy7	BioLegend	clone: 1D3; cat#: 115530; lab: Benoist
CD24 Fitc	BioLegend	clone: M1/69; cat#: 101806; lab: Benoist
CD25 APC	BioLegend	clone: PC61; cat#: 101910; lab: Benoist
CD25 PE	BioLegend	clone: PC61; cat#: 101904; lab: Benoist
CD28 Bio	BioLegend	clone: E18; cat#: 102104; lab: Benoist
CD4 APC	eBiosciences	clone: RM4-5; cat#: 17-0042-82; lab: Benoist
CD4 PE	eBiosciences	clone: RM4-5; cat#: 12-0042-82; lab: Benoist
CD44 Fitc	BioLegend	clone: IM7; cat#: 103022; lab: Benoist
CD45 PE CF594	BioLegend	clone: 30 F11; cat#: 562420; lab: Benoist

Continued

REAGENT or RESOURCE	SOURCE	IDENTIFIER
CD45 APC-Cy7	BioLegend	clone: 30 F11; cat#: 103116; lab: Benoist
CD45R P.B.	BioLegend	clone: RA3 6B2; cat#: 193227; lab: Benoist
CD62L PE-Cy7	BioLegend	clone: MEL14; cat#: 104418; lab: Benoist
CD69 A700	BioLegend	clone: H1.2F3; cat#: 104539; lab: Benoist
CD8 A700	BioLegend	clone: 53 6.7; cat#: 100730; lab: Benoist
CD8 PE-Cy7	BioLegend	clone: 53 6.7; cat#: 100722; lab: Benoist
CD8 APC	BioLegend	clone: 53 6.7; cat#: 100712; lab: Benoist
EpCAM APC	BioLegend	clone: G8.8; cat#: 118214; lab: Benoist
F4/80 APC-Cy7	BioLegend	clone: BM8; cat#: 123118; lab: Benoist
F4/80 PE-Cy7	BioLegend	clone: BM8; cat#: 123114; lab: Benoist
F4/80 PE	BioLegend	clone: BM8; cat#: 123110; lab: Benoist
Ly6G/Gr1 APC-ef780	eBiosciences	clone: RB6 8C5; cat#: 47-5931-82; lab: Benoist
Ly6G/Gr1 APC-Cy7	BioLegend	clone: RB6 8C5; cat#: 108424; lab: Benoist
Ly6G/Gr1 APC	BioLegend	clone: RB6 8C5; cat#: 108412; lab: Benoist
ICAM2/CD102 Fitc	eBiosciences	clone: mIC2/4; cat#: 11-1029-42; lab: Benoist
IgM Fitc	eBiosciences	clone: eB121 15F9; cat#: 11-5890-82; lab: Benoist
Ly51 PE	BioLegend	clone: 6C3; cat#: 108308; lab: Benoist
MHCII Fitc	BioLegend	clone: M5/114; cat#: 107606; lab: Benoist
NK1.1 APC-Cy7	BioLegend	clone: PK136; cat#: 108710; lab: Benoist
NK1.1 APC	BioLegend	clone: PK136; cat#: 108724; lab: Benoist
Nrp1 APC	BioLegend	clone: 3E12; cat#: 145206; lab: Benoist
TCRb ef450	eBiosciences	clone: H57 597; cat#: 47-5961-82; lab: Benoist
TCRb PE-Cy7	BioLegend	clone: H57 597; cat#: 109222; lab: Benoist
TCRb P.B.	BioLegend	clone: H57 597; cat#: 109226; lab: Benoist
TCRb PerCPcy5.5	BioLegend	clone: H57 597; cat#: 109228; lab: Benoist
TCRgd PerCPcy5.5	BioLegend	clone: GL3; cat#: 118118; lab: Benoist
Ter119 APC-ef780	eBiosciences	clone: Ter119; cat#: 47-5921-82; lab: Benoist
Ter119 APC-Cy7	BioLegend	clone: Ter119; cat#: 116223; lab: Benoist
CD45-APC-cy7	Biolegend	clone: NA; cat#: NA; lab: Colonna
CD3-FITC	Biolegend	clone: NA; cat#: NA; lab: Colonna
CD19-FITC	eBioscience	clone: NA; cat#: NA; lab: Colonna
THy1.2-APC	eBioscience	clone: NA; cat#: NA; lab: Colonna
TCRb-PE	PharMingen/BD	clone: NA; cat#: NA; lab: Colonna
KLRG1-PE	Biolegend	clone: NA; cat#: NA; lab: Colonna
CD5-PE	Biolegend	clone: NA; cat#: NA; lab: Colonna
CCR6-BV421	PharMingen/BD	clone: NA; cat#: NA; lab: Colonna
NKp46-biotin	Colonna Lab	clone: NA; cat#: NA; lab: Colonna
CD3-PercP-Cy5.5	eBioscience	clone: NA; cat#: NA; lab: Colonna
CD19-PercP-Cy5.5	ebioscience	clone: NA; cat#: NA; lab: Colonna
NK1.1-PercP-Cy5.5	Biolegend	clone: NA; cat#: NA; lab: Colonna
SCA1-PacBlue	Biolegend	clone: NA; cat#: NA; lab: Colonna
CD127-FITC	eBioscience	clone: NA; cat#: NA; lab: Colonna
KLRG1-APC	eBioscience	clone: NA; cat#: NA; lab: Colonna

Continued

REAGENT or RESOURCE	SOURCE	IDENTIFIER
ST2-biotin	eBioscience	clone: NA; cat#: NA; lab: Colonna
SAV-PE-Cy7	eBioscience	clone: NA; cat#: NA; lab: Colonna
CD3e PE	eBioscience	clone: 145-2C11; cat#: 12-0031-82; lab: Randolph
CD3e PECy7	eBioscience	clone: 145-2C11; cat#: 25-0031-82; lab: Randolph
CD11b APCCy7	Biolegend	clone: M1/70; cat#: 101226; lab: Randolph
CD19 PE	Biolegend	clone: 6D5; cat#: 115508; lab: Randolph
CD45 PB	Biolegend	clone: 30-F11; cat#: 103126; lab: Randolph
CD64 APC	BD Biosciences	clone: X54-5/7.1; cat#: 558539; lab: Randolph
CD102 (ICAM2) Alexa 488	eBioscience	clone: 3C4; cat#: 53-1021-82; lab: Randolph
CD115 PE	eBioscience	clone: AFS98; cat#: 12-1152-82; lab: Randolph
CD115 APC	eBioscience	clone: AFS98; cat#: 17-1152-82; lab: Randolph
CD206 FITC	Biolegend	clone: C068C2; cat#: 141704; lab: Randolph
CD226 PE	Biolegend	clone: 1000000; cat#: 128806; lab: Randolph
B220 PECy7	eBioscience	clone: RA3-6B2; cat#: 25-0452-82; lab: Randolph
Ly6C BV421	Biolegend	clone: HK1.4; cat#: 128032; lab: Randolph
Ly6G PE	BD Biosciences	clone: 1A8; cat#: 553128; lab: Randolph
Ly6G PE-Cy7	BD Biosciences	clone: 1A8; cat#: 560601; lab: Randolph
F4/80 FITC	Biolegend	clone: BM8; cat#: 123108; lab: Randolph
F4/80 PE-Cy7	Biolegend	clone: BM8; cat#: 123114; lab: Randolph
MHCII (I-A/I-E) PB	Biolegend	clone: M5/114.15.2; cat#: 107620; lab: Randolph
MerTK PECy7	eBioscience	clone: DSSMMER; cat#: 25-5751-82; lab: Randolph
CD3 Biotin	Biolegend	clone: 145-2C11; cat#: 100304; lab: Wagers
CD4 Biotin	Biolegend	clone: GK1.5; cat#: 100404; lab: Wagers
CD5 Biotin	ebioscience	clone: 53-7.3; cat#: 12-0051-85; lab: Wagers
CD8 Biotin	Biolegend	clone: 53-6.7; cat#: 100704; lab: Wagers
CD19 Biotin	Biolegend	clone: 6D5; cat#: 115504; lab: Wagers
B220 Biotin	Biolegend	clone: RA3-6B2; cat#: 103204; lab: Wagers
GR-1 Biotin	ebioscience	clone: RB6-8C5; cat#: 13-5931-82; lab: Wagers
Mac-1 Biotin	ebioscience	clone: M1/70; cat#: 13-0112-85; lab: Wagers
Ter-119 Biotin	Biolegend	clone: TER-119; cat#: 116204; lab: Wagers
Streptavidin Pacific Orange	Thermo Fisher	clone: NA; cat#: S32365; lab: Wagers
Sca-1 PECy7	Biolegend	clone: D7; cat#: 108113; lab: Wagers
c-Kit APC	ebioscience	clone: 2B8; cat#: 17-1171-83; lab: Wagers
CD48 APCCy7	Biolegend	clone: HM48-1; cat#: 103431; lab: Wagers
CD150 PE	Biolegend	clone: TC15-12F12.2; cat#: 115904; lab: Wagers

Continued

REAGENT or RESOURCE	SOURCE	IDENTIFIER
CD34 FITC	ebioscience	clone: RAM34; cat#: 11-0341-85; lab: Wagers
Flk2 PEcf594	BD biosciences	clone: A2F10.1; cat#: 562537; lab: Wagers
Biological Samples		
Sorted cell populations	This paper	Table S1 and http://www.immgen.org/ImmGenATAC1219Sorts.S1A.pdf
Critical Commercial Assays		
Nextera DNA Library Preparation Kit	Illumina	FC-121-1030
Deposited Data		
Raw sequencing data	This paper	GEO: GSE100738
Experimental Models: Organisms/Strains		
C57BL/6 mice	Jackson Laboratory	Jax0664
B6.Rorc^{tm2Litt}	Jackson Laboratory	Jax7572
Foxp3-ires-gfp reporter mice		PubMed: 16648838
Software and Algorithms		
Genome mm10	http://hgdownload.cse.ucsc.edu/goldenpath/mm10/bigZips/mm10.2bit	mm10
Transcription start sites	http://hgdownload.cse.ucsc.edu/goldenPath/mm10/database/refFlat.txt.gz	downloaded Jan. 2017
Blacklisted regions	http://mitra.stanford.edu/kundaje/akundaje/release/blacklists/mm10-mouse/mm10.blacklist.bed.gz	N/A
RNaseq GTF file	https://genome.ucsc.edu/cgi-bin/hgTables	N/A
Genome conservation scores	http://hgdownload.cse.ucsc.edu/goldenpath/mm10/phastCons60way/mm10.60way.phastCons.bw	N/A
sickle1.2 (Version 1.33)		https://github.com/najoshi/sickle
TrimGalore version 0.4.0	http://www.bioinformatics.babraham.ac.uk/projects/trim_galore/	
Bowtie2	http://bowtie-bio.sourceforge.net/bowtie2/index.shtml	
Samtools 0.1.19	http://samtools.sourceforge.net	
Picard Tools	http://broadinstitute.github.io/picard/	N/A
hisat2 version 2.0.4	https://ccb.jhu.edu/software/hisat2/manual.shtml	
Htseq version 0.6.1	https://htseq.readthedocs.io/en/release_0.10.0/	
Gaston version 1.5.3	https://cran.r-project.org/web/packages/gaston/index.html	
IGV	http://software.broadinstitute.org/software/igv/	
MACS2	https://github.com/taoliu/MACS/wiki	
BEDTools	https://bedtools.readthedocs.io/en/latest/	Quinlan and Hall, 2010
HOMER	http://homer.ucsd.edu/homer/	
chromVAR	https://bioconductor.org/packages/release/bioc/html/chromVAR.html	Schep et al., 2017
chromVARmotifs version 0.2.0	https://github.com/buenrostrolab/chromVARmotifs	Schep et al., 2017
Other		
H3K4Me1 ChIP-seq	Placek et al., 2017	GSE69162
FoxP3 ChIP-seq	Samstein et al., 2012	GSE40684

(*Continued on next page*)

Continued

REAGENT or RESOURCE	SOURCE	IDENTIFIER
FoxP3, H3K27Ac, H3K4Me1/3, Mediator, Cohesin ChIP-seq	Kitagawa et al., 2017	DRA003955
PAX5 ChIPseq	Revilla-I-Domingo et al., 2012	GSE38046
RORγ ChIPseq	Guo et al., 2016	GSE88916

CONTACT FOR REAGENT AND RESOURCE SHARING

Further information and requests for resources and reagents should be directed to the Lead Contact, Christophe Benoist (cbdm@hms.harvard.edu).

EXPERIMENTAL MODEL AND SUBJECT DETAILS

Mice

C57BL/6 mice were obtained from the Jackson Laboratory, as were B6.Rorc[tm2Litt] (Jax7572), housed under SPF conditions (HMS IACUC protocol 02954). Young adult males or females (as listed in Table S1) were used at 5-6 weeks of age. Rorc-deficient mice were generated in (+/− x +/−) crosses, and +/+ or +/− littermates were used as controls.

METHOD DETAILS

ATAC-seq Data Generation

To ensure consistency in the data, the different immune cell populations were sorted and frozen in each participating laboratory, but all processing, library construction and sequencing were performed jointly in the ImmGen core lab. As a pilot for this multi-site program, all participating labs generated samples of total splenic CD19+ B cells, a readily sorted cell population (which led to some refinement of the procedure and provided a baseline of inter-replicate variance).

Mice were sacrificed and immunocytes were isolated to high purity by flow cytometry according to ImmGen SOP using the antibodies and gates indicated in Table S1 and Figure S1A. two rounds of sorting were performed to collect 10,000 cells (exceptions for Cd34-LTHSC, Cd34+LTHSC and STHSC populations for which 677, 2483 and 3660 cells were sorted, respectively) in 1.5mL DNA lobind tubes (#022431021, Eppendorf) containing 100uL of BAMBANKER (serum-free cell freezing medium, No.302-14681, Wako). Cells were kept on ice at most 30 minutes and immediately stored at −80°C following a slow-freeze procedure; (cell freezing container with isopropyl alcohol at a rate of −1°C/minute with temperatures decreasing from 4°C to −80°C).

ATAC-seq libraries were prepared as previously reported (Corces et al., 2016) with the following modifications. Frozen cells were thawed, washed with 1mL of PBS containing protease inhibitors (Complete EDTA-free protease inhibitor cocktail, Roche Diagnostics, Basel, Switzerland) and cell pellets were resuspended in 10uL of Tn5 transposase mixture: 1x Tagment DNA Buffer, 0.5uL Tagment DNA Enzyme (Nextera DNA Library Preparation Kit, Illumina) and 0.2mg/ml digitonin (#G9441, Promega) on ice. Cells were incubated at 37°C for 30 minutes with agitation followed by DNA isolation using the MinElute Reaction Cleanup Kit (QIAGEN, Hilden, Germany). Construction of ATAC-seq libraries included an initial round of PCR in a total volume of 50uL using the NEBNext High-Fidelity 2X PCR Master Mix (New England Biolabs, MA, USA) with primers (0.5uM each) from (Buenrostro et al., 2015) with the following thermal cycles: 5 minutes at 72°C, 30 s at 98°C, followed by 7 cycles [98°C for 10 s, 63°C for 30 s and 72°C for 60 s] and a final extension at 72°C for 5 minutes. PCR products were purified and size-selected using Agencourt AMPure XP beads (Beckman Coulter) (0.65x and 1.8x volume to remove long and short fragments respectively) and eluted in 18uL of EB (QIAGEN). To avoid over amplification of libraries which result in GC bias, 2uL of the eluted DNA were subjected to qPCR (StepOnePlus Real-Time PCR System, Life Technologies) in a volume of 20uL using SYBR GreenI dye (final 0.6x SYBR GreenI, Life Technologies) and with the respective primers (1.25uM each), as performed in the first round of PCR. Following qPCR [30 s at 98°C, followed by 30 cycles (98°C for 10 s, 63°C for 30 s and 72°C for 60 s)], amplification curves were analyzed and the optimal number of PCR cycles for each sample were estimated with cycle thresholds reaching ¼ of the maximum. Upon selecting the cycle threshold, 12.5uL of the eluted DNA were subjected to a second round of PCR in a volume of 50uL with NEBNext High-fidelity 2x PCR master mix, respective primers (1.25uM each) and the following thermal cycles: 30 s hot-start at 98°C, followed by 7∼13 cycles [98°C for 10 s, 63°C for 30 s and 72°C for 60 s] and a final extension at 72°C for 5 minutes. The libraries were purified by Agencourt AMPure XP beads (x1.8 vol.), quantified by qPCR using Power SYBR Green PCR Master mix (ThermoFisher) and universal sequencing primers (P5_FW:5′AATGATACGGC GACCACCGA and P7_RV:5′CAAGCAGAAGACGGCATACGA, 0.2uM each) and pooled, which were sequenced as paired-end (38+37bp) on an Illumina NextSeq 500 instrument in high-output mode.

ATAC-seq Quantification and Normalization

After trimming adaptor sequences and low quality reads using sickle1.2 (https://github.com/najoshi/sickle), short reads were mapped to mm10 reference genome using bowtie2 with the following options; -X 1000 –fr, while non-unique, ChrM mapping (0.1~20%, median = 4.1%) and duplicated reads (7~69%, median = 22%) were filtered out using samtools view -q 30 [samtools 0.1.19] and Picard Tools (Picard MarkDuplicates, http://broadinstitute.github.io/picard). The summary of ATAC-seq read statistics can be found in Table S1. Paired-end reads spanning less than 120 bp were used for determining the peak summits in all populations using MACS2 functions (–call-summits) (https://github.com/taoliu/MACS). Open chromatin regions (OCR) of a 250 bp width were centered on all summits selecting the peak summit with the most significant q-value, when compared with ATAC-seq signals in 332,233 regions. Formally, 2 to 181 samples were grouped according to a hierarchical clustering with various cut-offs in order to achieve sequencing depth and estimate the peak summits for all populations. A window of 250 bp was used onset based off centered summits similarly in the first step, which resulted in 518,845 ATAC-seq OCRs. As some OCRs can arise as sequencing-based artifacts (ENCODE Project Consortium, 2012) and may also share sequence homology with the mitochondrial genome, we removed possible artifact OCRs by filtering blacklisted genomic regions and chrM homologous regions (a blacklist was downloaded from: https://sites.google.com/site/anshulkundaje/projects/blacklists).

ChrM homologous regions were identified by mapping short mitochondrial DNA sequences to the mouse nuclear chromosomes, consisting of 7,889 genomic regions in total. We report 512,595 cumulative OCRs (ImmGenATAC1219.peak_1 ~512595) across our cis-regulatory atlas. For the analysis of TSS (transcriptional start sites) and DE (distal enhancers) connected OCRs, we designated these OCRs as TSS connected (i.e., OCRs of which summit is within 125bp upstream or downstream of TSS, as all OCRs are 250bp width centered on the summit) and all others as DE connected OCRs. 27,921 TSS positions were defined from UCSC annotation data on mm10 (http://hgdownload.cse.ucsc.edu/goldenPath/mm10/database/refFlat.txt.gz, downloaded Jan. 2017). We employed the same reference data to assign close-by genes for each OCR as reported in Table S2.

To compute signal intensity in each OCR, reads mapped to the plus strand were shifted by +4 bp and reads mapped to the minus strand by −5 bp. Second, edges of fragments corresponding to paired reads were tested for OCR overlapping using BEDTools2.25.0 [bedtools intersect (Quinlan and Hall, 2010)]. A fragment edge in an OCR was counted unless the other edge of the fragment mapped to the same OCR in order to avoid counting non-independent Tn5 insertion events. A pseudo count of 0.1 was added to edge counts in peaks, log2-transformed and normalized by quantile normalization. For calculating the cell population mean, the quantile-normalized counts were converted back to linear scale and means of replicates were calculated (Table S2A). Backgrounds were estimated based on the ATAC-seq signals of regions through random sampling with p values for each OCR computed using a negative binominal distribution of the background in each sample. Data were also adjusted for multiple hypothesis testing using the Benjamini and Hochberg (BH) method. All population p values are supplied in Table S2.

Replicates for each population were merged and paired reads spanning less than 120 bp regions were used to compute ATAC-seq pile-up traces for each population using MACS2, which were further normalized by quantile normalization across 25bp bins. To visualize the data, we used IGV (http://software.broadinstitute.org/software/igv/). The assembled data can be analyzed interactively on the USCS platform via the ImmGen Chromatin browser (http://rstats.immgen.org/Chromatin/chromatin.html).

ATAC-seq QC

Data quality control analyses were performed for each sample and across the projects by: (1) counting the number of properly mapped paired ends, setting a threshold of 2,470,102 as acceptable across this project (range 2,470,102 to 16,029,540, median 6,841,995). (2) computing signal enrichments around the TSS relative to genomewide average, a metric which identifies datasets with high signal to noise ratios (Corces et al., 2016) (Table S1); a value > 3.9% was considered acceptable across this project (range 3.9% to 31.8%, median 12.5%). (3) Concordance between the two biological replicates. We selected, for each cell-type, a subset of OCRs in which the raw edge counts were > = 10 in at least one replicate, which was used to compute a Pearson correlation between the two replicates. The Pearson coefficient is sensitive to the total number of reads (as evidenced by the B cell pilot, Figure S1B left). The samples retained for the analysis exhibited comparable inter replicates correlations to the trend estimated from B cell pilots (green line, Figure S1B right).

RNA-seq

RNA-seq was performed with the standard ImmGen low-input protocol. A total of 1,000 cells were sorted directly into 5ul of lysis buffer (TCL Buffer (QIAGEN) with 1% 2-Mercaptoethanol). Smart-seq2 libraries were prepared as previously described (Picelli et al., 2014) with slight modifications. Briefly, total RNA was captured and purified on RNAClean XP beads (Beckman Coulter). Poly-adenylated mRNA was then selected using an anchored oligo(dT) primer (5′–AAGCAGTGGTATCAACGCAGAGTACT30VN-3′) and converted to cDNA via reverse transcription. First strand cDNA was subjected to limited PCR amplification followed by Tn5 transposon-based fragmentation using the Nextera XT DNA Library Preparation Kit (Illumina). Samples were then PCR amplified for 18 cycles using barcoded primers such that each sample carries a specific combination of eight base Illumina P5 and P7 barcodes for subsequent pooling and sequencing. Paired-end sequencing was performed on an Illumina NextSeq 500 using 2 × 25bp reads.

Low quality reads were trimmed using sickle1.2 and the adaptor sequence with TrimGalore (version0.4.0, http://www.bioinformatics.babraham.ac.uk/projects/trim_galore/). Short reads were then mapped to mm10 genome using hisat2 [version2.0.4 (https://ccb.jhu.edu/software/hisat2/manual.shtml)] with–transcriptome-mapping-only–no-discordant options. Unmapped and low

quality scoring (MAPQ < 5) reads were removed using samtools. Moreover, duplicated reads were removed using the Picard MarkDuplicates function. Properly paired reads were selected by samtools view -f 0x02 and counted for each gene using htseq-count (version0.6.1) with -s no option and a GTF file from UCSC mm10 refGene downloaded from UCSC table browser (https://genome.ucsc.edu/cgi-bin/hgTables). Genes with a minimum read count of 5 in all replicates of a population (17,535 genes) were retained. A pseudo count of 1 was added and log2-transformed prior to quantile normalization. Quantile-normalized counts were converted back to a linear scale and means of replicates were calculated for each population (Table S2C). The number of reads for each processing step can be found in Table S1B.

QUANTIFICATION AND STATISTICAL ANALYSIS

Dimensionality Reduction and Visualization with t-SNE

To visualize the 334,879 OCRs sampled from our collection of populations, we performed a t-Stochastic Neighbor Embedding of the OCR x cell-type count matrix. Specifically, we derived the top 25 principal components from the $334,870 \times 86$ matrix using the implicitly restarted Lanczos bidiagonalization algorithm (irlba). Next, we embedded this high-dimensional chromatin accessibility landscape into a two-dimensional coordinate system using the Barnes-Hut implementation of t-SNE through the Rtsne package with default parameters (perplexity = 30). Individuals peaks were assigned binary TF motif matches based on predicted binding affinities of the mm10 sequence and correspondingly colored (see below for motif matching analysis). For sample populations-based coloring, each peak was assigned a population with the maximum chromatin accessibility observed from the normalized counts matrix. Finally, for each peak i in our dataset, we computed the Gini Index over the n populations, yielding a per-peak measure of "chromatin inequality" about the populations. The Gini Index for peak i, denoted G_i, was computed as:

$$G_i = \frac{\sum_{j=1}^{n} \sum_{k=1}^{n} |x_{i,j} - x_{i,k}|}{2n \sum_{j=1}^{n} x_{i,j}}$$

where $x_{i,j}$ represents an element in the the $\log_2$ normalized counts matrix for peak i and population j.

OCR Variance Component Analysis

We applied variance component models to characterize how patterns of chromatin covariance (Figure 2A) explained observed gene expression variance within our sorted populations. As a variance components model assumes normally distributed noise, we utilized a variance stabilizing transformation proposed by Anscombe (1948) to model the empirical a negative binomial distribution of RNA-seq count data. Specifically, for each gene (indexed by i), the vector of normalized gene expression counts per cell-type, Y_i, was transformed into a new vector Y_i' from centering and scaling using Anscombe's transformation:

$$Y_i' = \left(\sqrt{\frac{Y_i + 3/8}{1/\phi - 3/4}} \right),$$

where ϕ is the dispersion chosen so as to minimize the ratio of the dispersion of the residual standard deviation as implemented in the Varistran package (https://github.com/MonashBioinformaticsPlatform/varistran). With our transformed gene expression vector j, we then fit the following variance component model:

$$Y_i' \sim N\left(0, D\sigma_d^2 + T\sigma_t^2 + I\sigma_e^2\right),$$

where D and T are the sample-sample correlation matrices computed from the distal enhancers and transcription start site OCRs respectively (see Figure 2A) and I is the identify matrix. Average information restricted likelihood estimation (AIREML) was used to estimate the values of the parameters of the variance component models, σ_d, σ_t, and σ_e. To then determine the proportion of the variance explained by each variance component, we generated a vector V_i, which by definition sums to 1:

$$V_i = \left\langle \frac{\sigma_d^2}{\sigma_d^2 + \sigma_t^2 + \sigma_e^2}, \frac{\sigma_t^2}{\sigma_d^2 + \sigma_t^2 + \sigma_e^2}, \frac{\sigma_e^2}{\sigma_d^2 + \sigma_t^2 + \sigma_e^2} \right\rangle$$

Here, the proportion of the variance in expression for gene i explained by the DE logic would be represented by the first element in the V_i vector.

Associating OCRs with Target Genes

Data normalization and aggregation: We defined "expressed" genes as those with at least 10 reads in at least one cell population. Using this filter, we removed lowly expressed genes, and retained expression data for 15,601 genes. This filtered gene expression data was then log transformed, quantile normalized, and averaged across replicates. Similarly, ATAC-seq data was filtered to exclude OCRs with low intensity (BH adjusted MACS2 p value > 0.05). The intensities across the cell populations were log

transformed, quantile normalized, and averaged across replicates. We excluded Stromal cells from this analysis: because of the large biological differences, data from this population has very different distributional properties compare to the others.

Association analysis: In simple association analysis, for each expressed gene, we identified all OCRs that are within 1Mb of the gene's TSS. Then, for each gene and "cis" OCR pair, we computed the Pearson correlation coefficient and the associated p value to quantify the association between activity (intensity) of the OCR and expression level of the gene across all 81 cell populations (samples). We used Bonferroni correction, to adjust the resulting p values. In addition, we used stepwise regression to identify independently associated OCRs nearby each gene. For each gene, we performed stepwise regression analysis with the gene expression level of a particular gene as outcome and the intensity of OCRs within 100Kb of the corresponding gene as the predictors. Similarly, we accounted for multiple testing using Bonferroni correction.

Computing Aggregated OCR Scores
As demonstrated in Figure 3C, we observed a "distance biased" relationship between OCR intensity and gene expression levels, whereby those *cis* OCR that are closer to TSSs are more strongly associated with gene expression levels. On the basis of this observation, we constructed an aggregated OCR score for each gene as the inverse weighted sum of OCR intensities within 100Kb of its TSS. More specifically, for a given gene, each OCR within 100Kb of the gene's TSS was given a weight 1/d where d is the absolute distance (in bp) between the gene's TSS and the center of the OCR.

Annotating OCRs with motifs
To annotate OCRs with putative transcription factor binding motifs, we used the motifmatchr package as part of the chromVAR suite of tools (Schep et al., 2017). Motifs were defined from a set of curated mouse position weight matrices (PWMs) from the cisBP database (http://cisbp.ccbr.utoronto.ca/) publicly available at (https://github.com/buenrostrolab/chromVARmotifs). For each OCR and motif pair, we determined a binary annotation for compatibility of the motif PWM in the mm10 reference sequence from the OCR. Specifically, our background nucleotide frequency was the total nucleotide content over all OCRs, and a motif match was called for sequences with a p value $< 5 \times 10^{-6}$. Note that these choices are identical the defaults provided in the motifmatchr package.

Associating Aggregated Motif Scores with Transcription Factor Expression
Deviation scores, referred to as "TFBS accessibility scores" throughout the text, were calculated using chromVAR with the default parameters (Schep et al., 2017) and the chromVAR motif database "mouse_pwms_v2." To compute the correlation between scores and TF expression we excluded epithelial cells whose patterns were too divergent, then filtered TFs for motif-TF expression pairs, wherein the maximum TF expression in a measured cell type was greater than 4 (log2 scale), resulting in 430 TFs (see Table S5G for the full list of TF motif and expression pairs). To calculate correlation between deviation scores and TF expression, log2 transformed gene expression counts were correlated (Pearson) to raw deviation scores. To calculate the statistical significance of the correlation two permutation tests were performed: we either permuted the sample labels or the TF labels (100 permutations with replacement), P values were calculated using a z-test comparing the observed TF motif-expression correlation coefficient to the permuted correlation coefficient. Reported values represent the max (least significant) of the two permutation approaches, TFs with P values less than 0.1 are called as significant. Notably, we found the two permutation approaches provided correlated P values however, permuting TFs labels generally provided less significant P values.

To compute correlation for myeloid and lymphoid TFs, the same approach was repeated for samples identified as lymphoid (LTHSC.34-.BM; LTHSC.34+.BM; STHSC.150-.BM; MMP4.135+.BM; preT.DN1.Th; preT.DN2a.Th; preT.DN2b.Th; preT.DN3.Th; DN4.Th; T.ISP.Th; T.DP.Th; T.4.Th; T.4.Nve.Sp; Treg.4.25hi.Sp; Treg.4.FP3+.Nrplo.Co; T.8.Th; T.8.Nve.Sp; T8.TN.P14.Sp; T8.TE.LCMV.d7.Sp; T8.MP.LCMV.d7.Sp; T8.Tcm.LCMV.d180.Sp; T8.Tem.LCMV.d180.Sp) or myeloid (Mo.6C+II-.Bl;Mo.6C-II-.Bl; MF.PC;MF.RP.Sp; MF.Alv.Lu;DC.103+11b-.SI; DC.103+11b+.SI; DC.4+.Sp;DC.8+.Sp; MF.microglia.CNS; GN.BM;GN.Sp;DC.pDC.Sp; MF.226+II+480lo.PC; MF.ICAM+480hi.PC) cell types.

Motif Enrichment in TSS
To determine motifs associated with DE-logic and TSS-logic genes identified from the variance components analysis (Figure 2), we performed two Fisher Exact tests per-motif. For each of the 15,600 expressed genes, we determined all motif matches from the motif collection within 1kb upstream of the annotated TSS. We then determined which motifs were enriched in the set of 943 TSS-logic genes from a first set of Fisher Tests (y axis Figure 2C), or enriched in the set of 4,409 DE-logic genes in a second set of Fisher Tests (x axis Figure 2C).

To assess of motif enrichment in selected sets of OCRs in the myeloid and T cell lineages (Figures 6 and S4) we employed a parametric test using motif frequency distributions calculated from GC-content matched background sets of OCRs, otherwise referred to as "chromVAR z-test for motif enrichment." First, after identifying OCRs to be tested (i.e., GN specific OCRs), 200 sets of GC-content matched OCRs were selected, using the 'getBackgroundPeaks' function from chromVAR, out of the robust set of 334,879 OCRs in the study. Background frequency distributions for each motif were then calculated from the background OCR sets using the OCR to motif pairing described above. Signed P values were then determined by the probability of obtaining the test set motif frequency in the background distribution and multiplying by the sign of the direction of effect, assuming a normal probability distribution for the background.

Analysis of Myeloid Lineage

Myeloid clustering and peak selection: OCRs were filtered for only those detected in at least one myeloid cell sample (BH adjusted MACS2 p value < 0.05; 215,583 peaks). The filtered peak signals (log2 + 1) were used for hierarchical clustering with 1 – Pearson correlation distance values and average linkage between clusters. Cell groups were formed by performing a tree cut on the dendrogram at a distance height of 0.21. Sets of peaks for each cluster were then identified by looking either for peaks specifically detected in a given cell group and no other myeloid cell types or for peaks with a minimum log2 peak signal fold change greater than 2 of that group compared to all other myeloid cells.

Myeloid motif enrichment: chromVAR z-test motif enrichment was performed on the selected sets of peaks for each group. Only the top 15 or fewer motifs having an unadjusted log10 signed p value greater than 5, and linear normalized gene counts greater than 100 in the population showing the enrichment were displayed in Figure 6B. SI macrophages not displayed due to lack of sequencing data.

cDC comparisons: Peaks for CD4 and CD8 DCs were selected by looking for peaks that were detected in one subset and not the other (BH adjusted MACS2 p value < 0.05), a minimum peak signal of 4, and a log2 peak signal fold change greater than 2 between the two cell types. chromVAR z-test motif enrichment was then run on these sets independently. The same analysis was run between the $CD103^+CD11b^+$ and $CD103^+CD11b^-$ DC populations in the SI.

Analysis of T Lineage

We identified 836 "T cell differentiation genes" whose expression varied the most during the T cell differentiation by combining the following groups: 1) 543 differential expressed genes by computing the mean and coefficient of variation from 12 cell populations along the T lineage ranging from MPP4.135+.BM to T.4.Nve.Sp and T.8.Nve.Sp and fitting generalized linear model on mean and squared CV (top 5% variable of the expressed genes); 2) 345 CD4 T cell related genes whose expression are significantly different between (MPP4 and STHSC) and (T.4.Th and T.4.Nve.Sp), (FC > = 5 or $\leq$ 0.2, P.value $\leq$ 0.05); and 3) 358 CD8 T cell related genes whose expression are significantly different between (MPP4 and STHSC) and (T.8.Th and T.8.Nve.Sp), (FC and P.value same as 2). Then, to examine the associated OCRs with these T cell genes, we targeted the most varied 1,232 OCRs within 10Kb from the TSS of these genes (TSS-OCRs were excluded and of 4,105 significant OCRs with P.value $\leq$ 0.05 in at least one population. For the analysis of Figure 5B, we excluded the constitutively open OCRs, and selected the 30% OCRs with highest variability through the T cell dataset (by fitting generalized linear model on mean versus squared CV of ATAC-seq signals).

For the analysis of OCR activation, we focused on the DE-OCRs with the highest positive correlation to each gene by computing Pearson's correlation between ATAC-seq signal and the corresponding gene expression within 12 T cell populations spanning differentiation from MPP4.135+.BM to T.4.Nve.Sp populations (because some genes had no correlated OCR within 10 Kb, 429 genes were retained). We then determined the population in which ATAC-seq signal and gene expression exceeded a 50% maximum and fell below 50% of the maximum along T cell differentiation. Genes were counted for the respective timing of OCR and gene activation/inactivation and represented as bubble plots in Figure 4B. Genes in which the expression was already maximum in MPP4.135+.BM progenitors were not considered in the analysis.

To relate TF expression and motif accessibility (Figures 7A–7C), OCRs containing a TF motif were selected from the table of significant OCRs (P.value $\leq$ 0.05 in at least one population) and 1,000 OCRs with the highest motif score were clustered using k-means. For TF motifs where ChIP-seq data are available at the NCBI GEO database, raw data were downloaded (https://www.ncbi.nlm.nih.gov/geo/, SRR4431502 and SRR4431506 for RORγ and SRR499696 $\sim$SRR499708 for Pax5) with a corresponding control data and analyzed by 1) mapping to mm10 reference using bowtie2, 2) discarding reads of non-unique mapping (samtools view -q 30), 3) removing duplicated reads by Picard.MarkDuplicates, 4) counting number of reads overlapping the OCRs, 5) normalizing reads by RPM (reads per million mapped reads) and 6) computing ChIP-seq signal as fold changes (ChIP-seq samples /control) after adding a pseudo count of 0.1.

FoxP3 Analysis

ChIP-seq datasets (Kitagawa et al., 2017), Database accession DRA003955 for H3K27Me3, H3K27Ac, H3K4Me1, H3K27Me3, Mediator and Smc1a (Cohesin) in Tregs were mapped to mm10 genome using bowtie. ChIP-seq peaks were called using HOMER (http://homer.ucsd.edu/homer/) with corresponding biological replicates and respective input controls. Additionally, H3K4Me1 ChIP-seq data was analyzed in the same manner for Tconv cells [(Placek et al., 2017), GSE69162]. A robust set of FoxP3 ChIP-seq binding sites were previously defined in Treg cells (Kwon et al., 2017). Briefly, fastq files (GSE40684, DRA003955) were mapped to the mm10 reference genome using bowtie. FoxP3 peaks from both studies were called using HOMER *findPeaks* function with an FDR of 1% using the parameter (*-style factor)* and respective input background peaks. Intersection of FoxP3 peaks were derived from both datasets Intersection of FoxP3 peaks were derived from both datasets using the BEDtools *intersect* function with a 50% reciprocal overlap requirement, yielding 5,047 robust FoxP3 peaks. Our analysis maps the cis-regulatory landscape during T cell differentiation for the top 2,000 FoxP3 ChIP-seq binding sites. FoxP3 peaks were parsed into promoter-proximal (920) and distal (1080) OCRs. Treg ChIP-seq histone mark and TF data were used to annotate all 2,000 FoxP3 peaks by binarizing each chromatin feature as being absent or present in each respective FoxP3 peak. Distal FoxP3 peaks were ordered based on accessibility differences Treg/LTHSC and Treg/DP. Distal FoxP3 OCRs were then parsed into constitutive (no differences in accessibility during T cell

differentiation; 860 peaks) or dynamic (> 2 fold ATAC-seq signal in at least one cell type upstream of Tregs; 220 peaks). TF motif enrichment was performed on FoxP3 constitutive and distal OCRs using chromVAR functions.
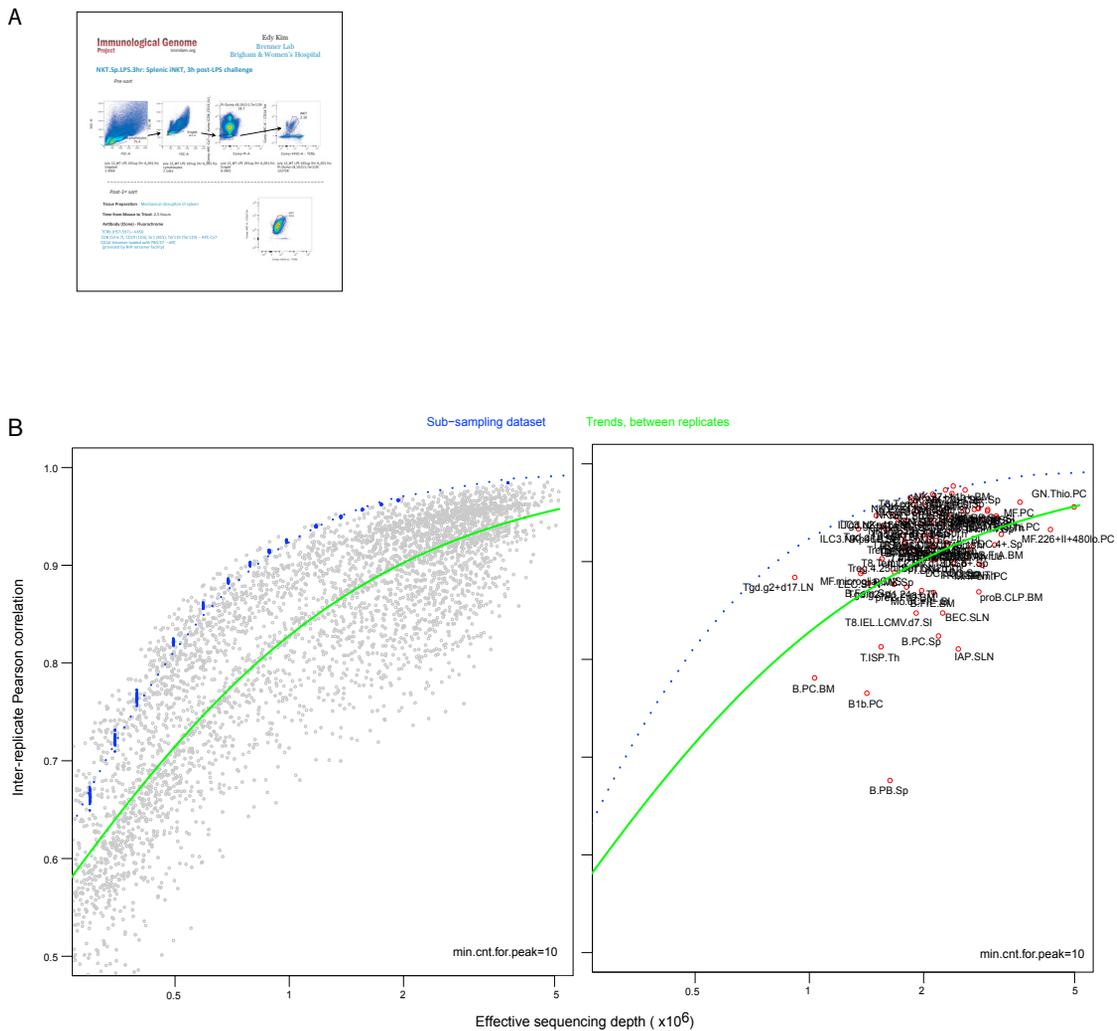
DATA AND SOFTWARE AVAILABILITY

The GEO accession number for the RNaseq and ATACseq data reported in this paper is GSE100738. Processed ATAC-seq data and called peaks can be found at:

https://sharehost.hms.harvard.edu/immgen/ImmGenATAC18_AllOCRsInfo.csv

Additional resources
The data can be visualized in the UCSC genome browser, the link to these data can be found here: http://rstats.immgen.org/Chromatin/chromatin.html.

A

B

Sub-sampling dataset   Trends, between replicates

Figure S1. Related to Figure 1

(A) Representative FACS page demonstrating cell isolations for profiling. The entire collection is assembled in a very large PDF which can be consulted at http://www.immgen.org/ATAC.Sort2017.pdf.

(B) Relationship between data depth and inter-replicate correlation. Left: Inter-replicate correlations for ATAC-seq signals in OCRs for splenic B cells (21 replicates of B.Sp, generated in different labs). Blue dots: optimal relationship between sequencing depth and inter-replicate correlation, computed by iterative subsampling of the entire merged B.Sp data. Subsampled data were applied to simulate the correlations in shallower depth and the trend line by a logistic regression model depicted in green. Blue dots indicate the correlations after different subsampling from all merged data with the trend line in blue. Right: Inter-replicate correlations for cell types employed in the analysis. The green line and the blue dotted line in the left panel are superimposed.
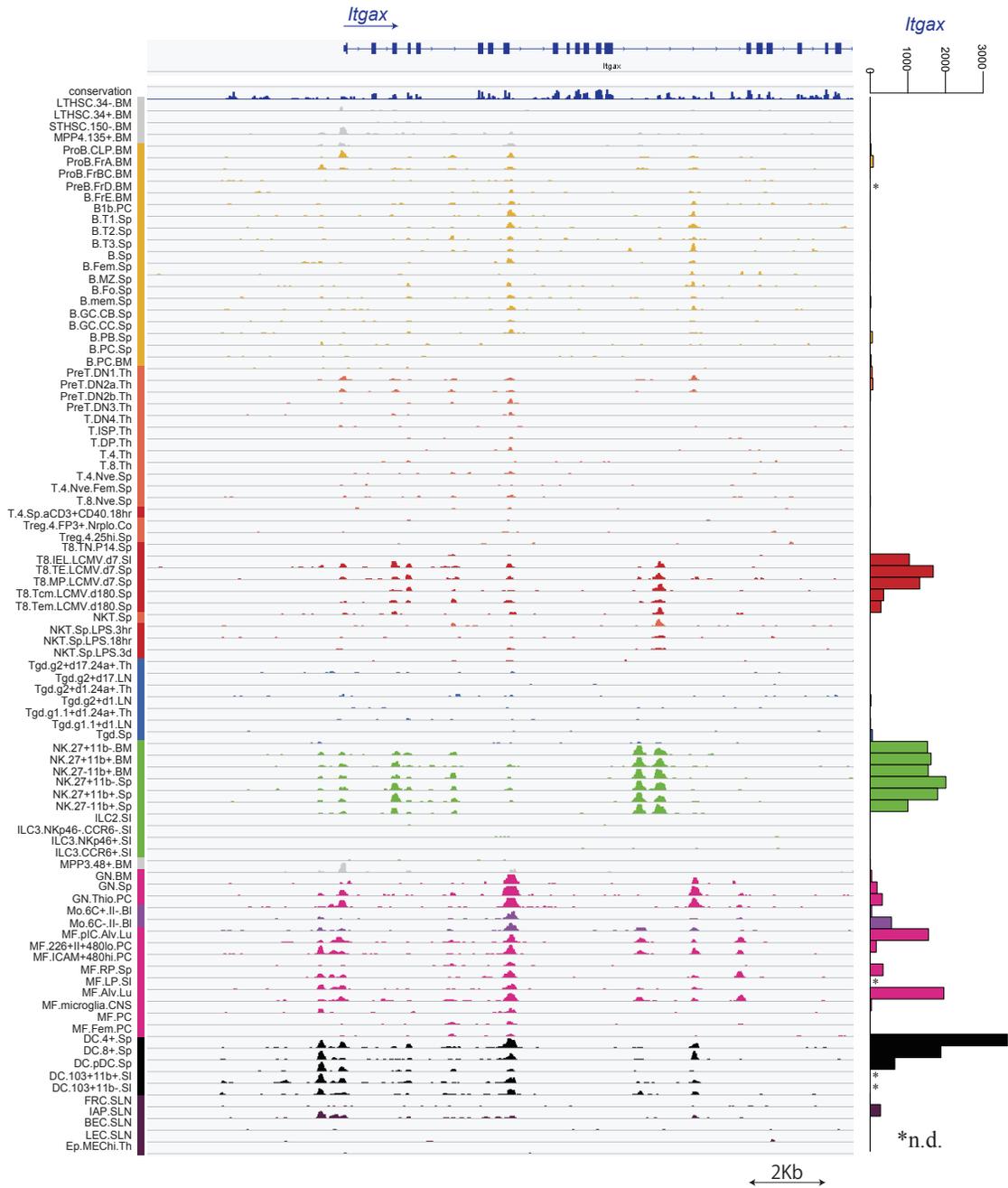
Figure S2. Related to Figure 1

Pile-up traces of ATAC-seq signals in Itgax locus. Blue bars in the first row indicate the positions of identified peaks (Pval ≤ 0.05) and the graph in the 2nd row conservation score among vertebrates. RNA expression for Itgax (Cd11c) gene are indicated by barplots with * where RNA-seq data was not acquired.
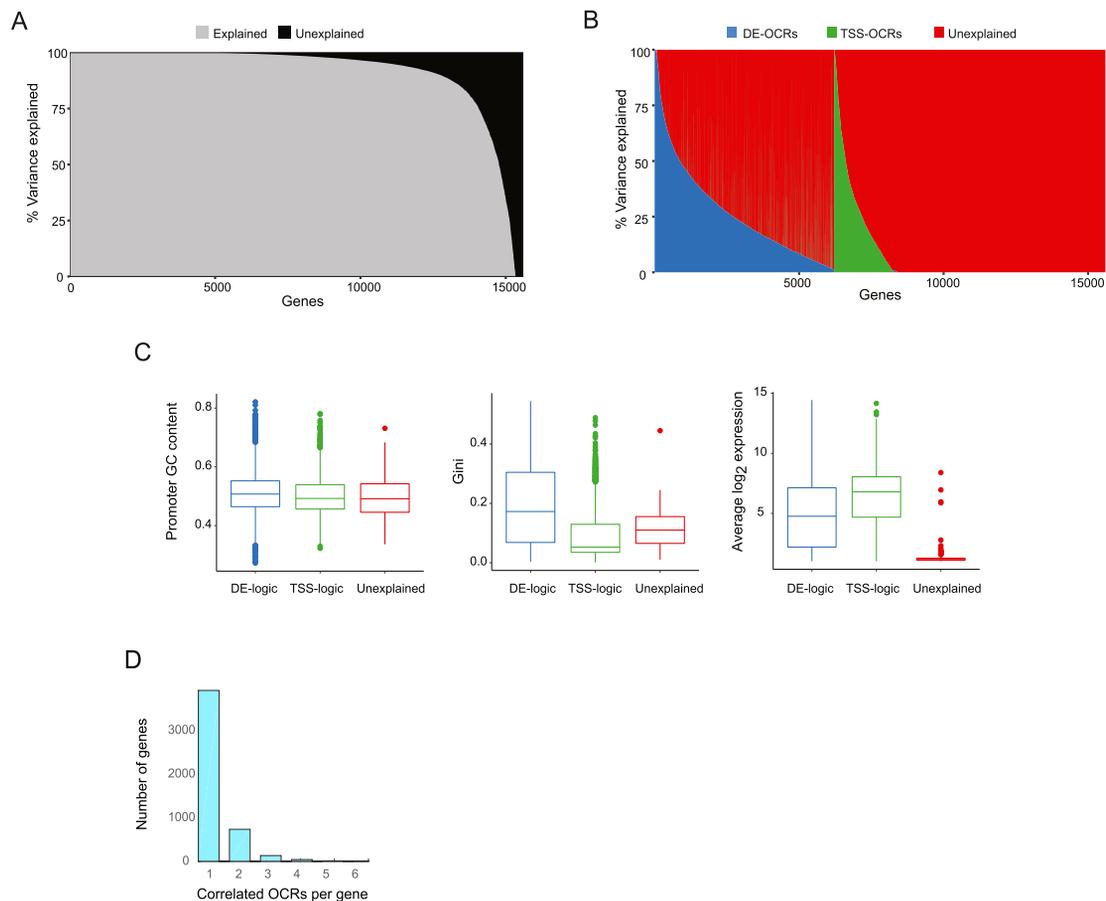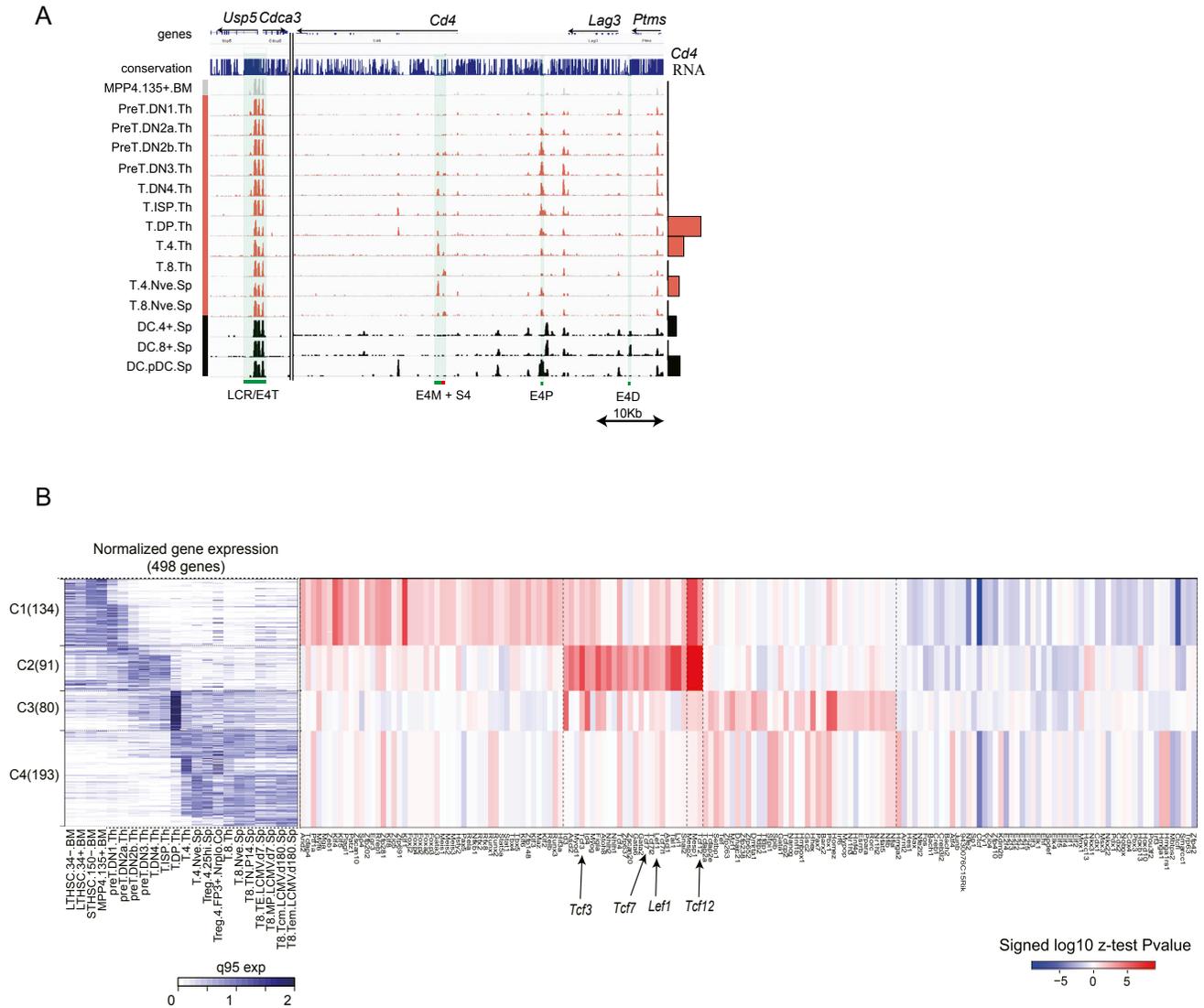
Figure S3. Related to Figure 2

(A) Summary of variance components results for each expressed gene using a single variance component of cell type relatedness from open chromatin data.

(B) Results of variance components model for two permuted matrices per gene model, showing minimal gene expression explained. Compare to Figure 2B.

(C) Attributes of genes where 99% of expression variance could be explained by DE (blue; n = 4,409) or TSS (green; n = 955) covariance. Genes in red (n = 223) had > 99% of variance unexplained from the variance components model. Shown are boxplots for promoter GC content, transcript inequality measured by the Gini Index, and mean log2 gene expression.

(D) Histogram of number of independent associated OCRs per gene. To determine independent associations, stepwise regression was used and the associated p values were adjusted for multiple testing using the Bonferroni approach.

A

B

Figure S4. Related to Figure 4

(A) Pile-up traces of ATAC-seq signals around Cd4 locus. Blue bars in the first row indicate the positions of identified OCRs and the graph in the 2nd row conservation score among vertebrates. RNA expression for Cd4 gene are indicated by barplots. LCR/E4T: locus control region/thymocyte enhancer, E4M: maturity enhancer, S4: silencer, E4P: proximal enhancer, E4D: distal enhancer

(B) TF motif enrichment (Left) normalized gene expressions for differentially expressed genes displayed after k-means clustering, same as Figure 4A (Right) Enriched TF binding motif in most variable OCRs within 10Kb from TSS for genes in each cluster (same set of OCRs as in Figure 4B) ChromVAR z-test motif enrichment was performed and motifs having an p value greater than or equal to 0.05 are displayed after k-means clustering.
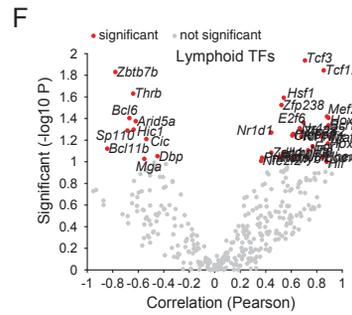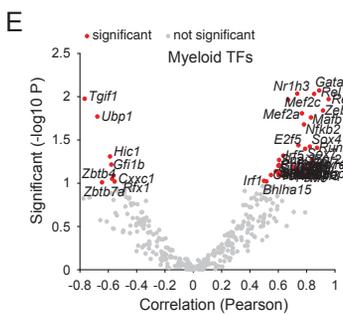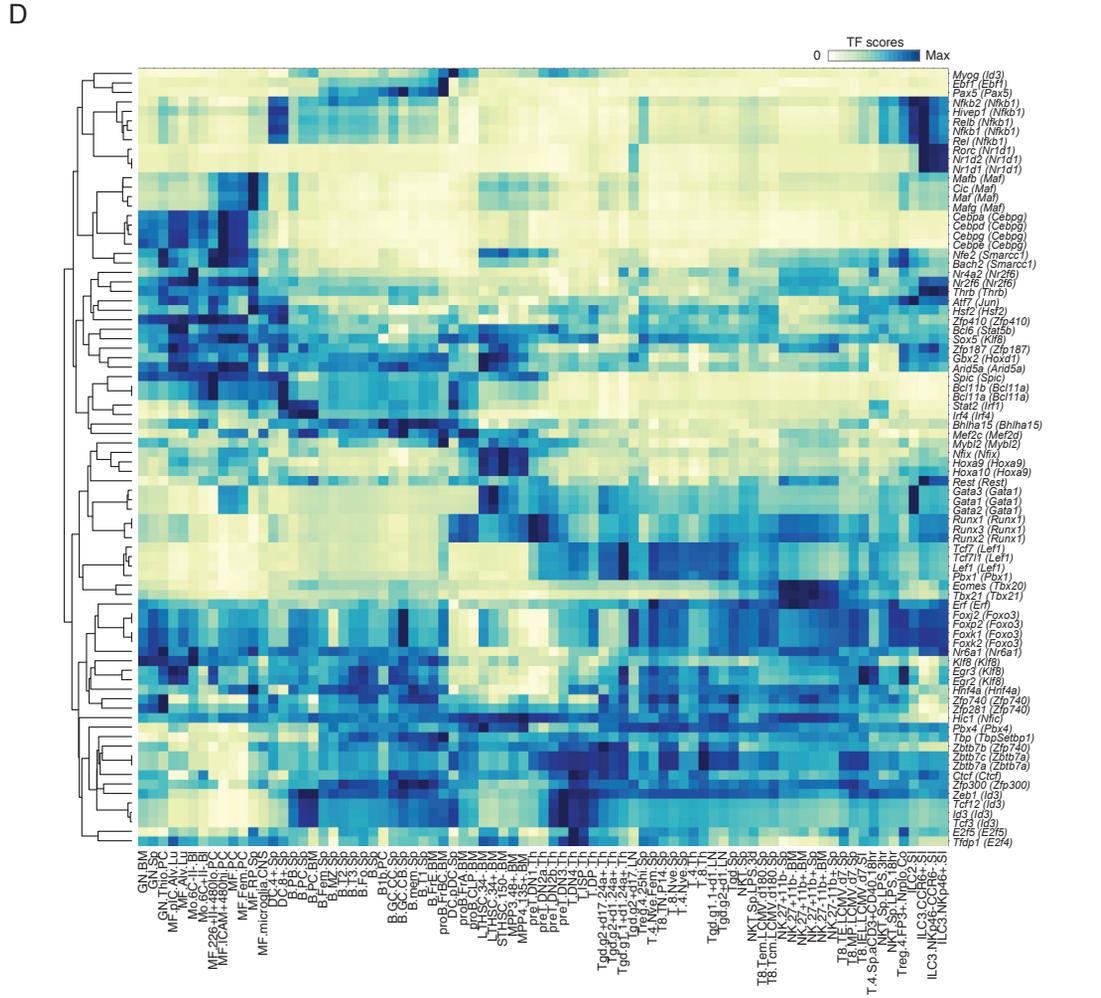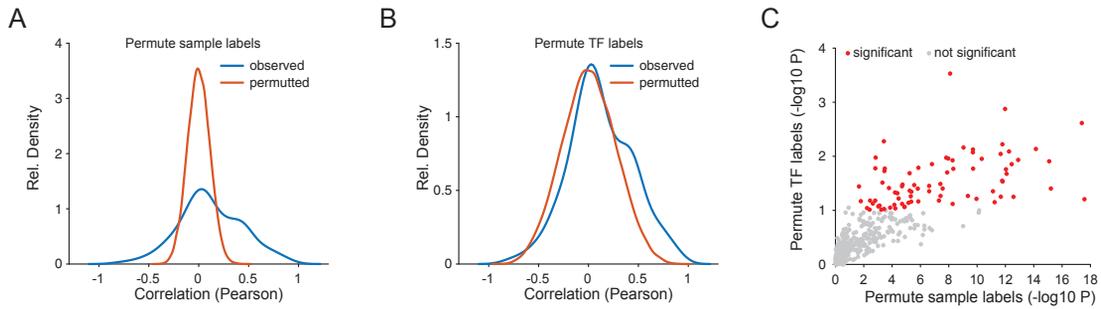
(legend on next page)

Figure S5. Related to Figure 5

(A and B) Correlation of expression and TF motif accessibility scores and permuted correlation, permuted either by their (A) sample labels or (B) TF labels.

(C) –log10 p values for TF expression and motif accessibility scores after permutation of the sample or TF labels.

(D) Hierarchical clustering for significantly correlated TF motif accessibility scores, motif name is labeled, motif family is denoted by parentheses.

(E and F) Correlation by –log10 p value of TF expression and motif accessibility scores filtering for (E) myeloid or (F) lymphoid samples.

A

Ehf expression

B
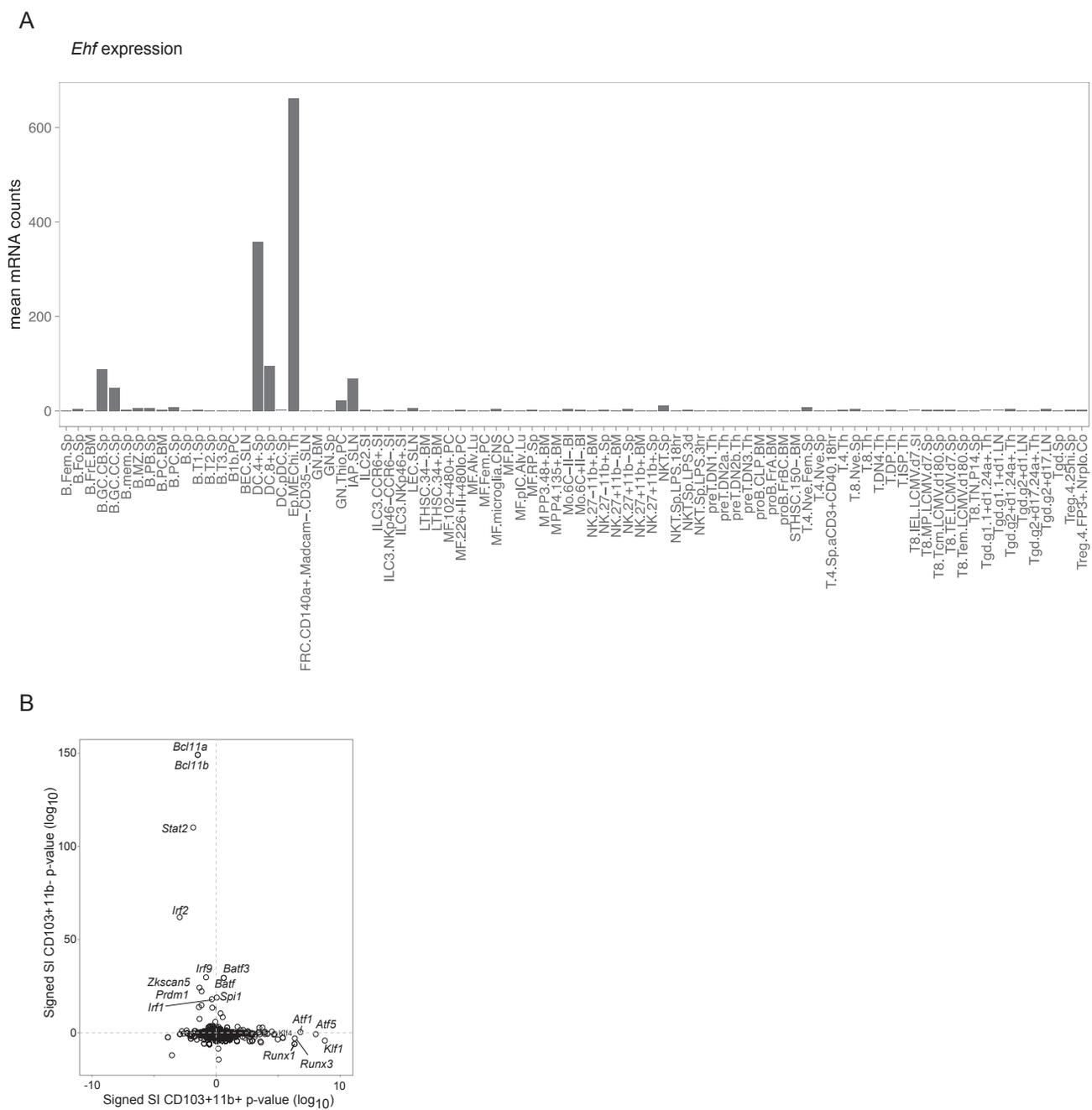
Figure S6. Related to Figure 6

(A) ChromVAR z-test motif enrichment for distinct peaks between CD103+CD11b+ and CD103+ CD11b- DCs.

(B) Mean Ehf mRNA counts from RNA-seq data in all samples profiled.
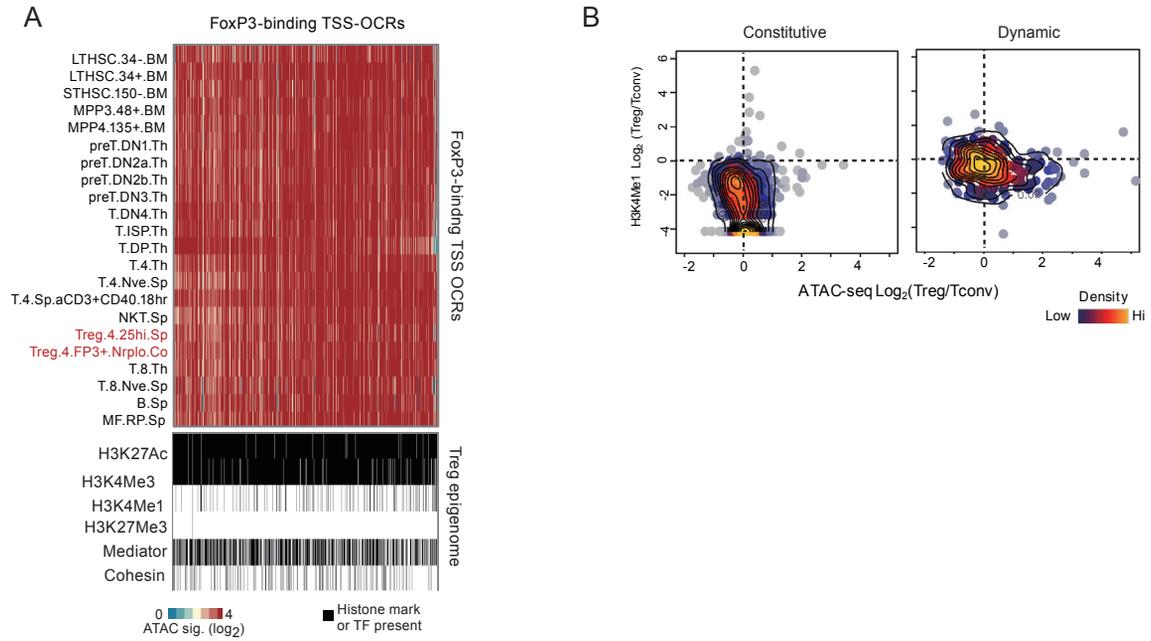
Figure S7. Related to Figure 7

(A) Constitutive chromatin accessibility (log2 ATAC-seq signal) for FoxP3 bound TSS OCRs (920). ChIP-seq data in Tregs for H3K27Ac, H3K4Me1, H3K4Me3, H3K27Me3, Mediator and Cohesin are marked as being present or absent for each respective TSS OCR.

(B) Chromatin accessibility (log2 Treg/Tconv ATAC-seq signal) and H3K4Me1 ChIP-seq (log2 Treg/Tconv ChIP-seq signal) from Treg and Tconv cells, reflects a shift in activity for dynamic FoxP3 OCRs.